Modulation of radiative heat transfer by higher-order topological phonon polaritons

Z. Gong,[1] B. X. Wang,[2,*] and C. Y. Zhao[1,†]

[1]*Institute of Engineering Thermophysics, School of Mechanical Engineering, Shanghai Jiao Tong University, Shanghai 200240, China*

[2]*2020 X-Lab, State Key Laboratory of Transducer Technology, Shanghai Institute of Microsystem and Information Technology, Chinese Academy of Sciences, Shanghai 200050, China*

(Received 17 December 2023; revised 15 August 2024; accepted 21 August 2024; published 11 September 2024)

Topological optical states are promising in waveguiding, sensing, and information processing which are localized over the boundaries and robustly protected by the band topology. Topological phonon polaritons (TPhPs), as a special type of topological optical states, have been shown to play a vital role in modulating radiative heat transfer in many-particle systems. In this paper, we propose subwavelength lattices composed of identical SiC nanoparticles (NPs) which support phonon polaritons to mimic the 2D Su-Schrieffer-Heeger (SSH) model. By using the coupled-dipole model and taking all the near- and far-field dipole-dipole interactions into account, we numerically calculate the band structures of the NP arrays under periodic boundary conditions (PBCs) and study the topological properties of the NP arrays characterized by their 2D Zak phases. Subsequently, we confirm the existence of edge states and high-order corner states in the topologically nontrivial 2D SSH lattices under open boundary conditions (OBCs), which are protected by the nonzero 2D Zak phases and consistent with the bulk-edge-corner correspondence. The radiative heat transfer between certain NPs is calculated based on many-body radiative heat transfer theory. We demonstrate that these high-order TPhPs can considerably modulate long-range radiative heat transport by constructing the topological "heat guiding" systems made of NP arrays with different boundary conditions. Moreover, by decomposing the radiative heat flux into two parts according to the polarization directions of dipoles, we find that the high-order TPhPs play different roles in the in-plane and out-of-plane components. We further show the modulation effect can robustly exist in the topologically nontrivial lattice by introducing defects and disorders. Our study provides an in-depth understanding on the near-field radiative heat transfer in many-particle systems with high-order topological properties.

DOI: 10.1103/PhysRevB.110.115419

I. INTRODUCTION

The discovery of topological phase of matter leads to a new perspective on the understanding and classification of condensed matter beyond the Landau's approach which characterizes states in terms of underlying symmetries [1]. In this paradigm, each gap in the band structure of matter can be labeled by its topological invariant, which describes the topological properties of matter [2,3]. One of the most important properties in this perspective is the existence of edge states at the interface between two systems with different topological invariants, which is immune against local perturbations due to the global robustness of the topological invariants. The novel edge states supported by the materials with topologically nontrivial properties, dubbed as "topologically protected edge states," provide potential applications in quantum computing and quantum storage for the resilience against control errors and perturbations [4–6], broadband and high-performance detectors [7–9], efficient and energy-saving field-effect transistors [10–12], etc. The relation between the topological properties and the emergence of edge states can be characterized by the bulk-boundary correspondence [13], i.e., n-dimensional (nD) topological insulators (TI) have $(n-1)$D localized edge states. Recently, high-order topological insulator (HOTI) has received growing interest as it supports edge states localized in lower dimension which goes beyond the conventional bulk-boundary correspondence [14–16]. To be specific, the mth-order TIs have nD gapped bulk states and $(n-1)$D, $(n-2)$D, ..., $(n-m+1)$D gapped edge states while having $(n-m)$D gapless edge states [17].

The high-order topology has been extensively studied in many other classical wave systems including acoustic [18,19], mechanical [20], phononic [21] systems, etc. In particular, the topological photonic system offers a fascinating platform for investigating high-order topology in which the topological behavior of electromagnetic wave can be well mimicked and experimentally observed in a relatively easier and highly controllable way. A number of studies regarding the high-order topological optical states have been carried out more recently. The topologically protected boundary states, which are localized in lower dimensions than predicted by the conventional bulk-boundary correspondence, can be supported in well-designed dielectric photonic crystals [17,22–26], plasmonic nanocavities [27,28] and nanoparticle arrays [29]. The proposed topological photonic systems have shown great capabilities in wave guiding [30,31], sensing [32,33], topological lasing [34], and information processing [35].

*Contact author: wangboxiang@mail.sim.ac.cn

†Contact author: changying.zhao@sjtu.edu.cn

Typical topological photonic systems are composed of discrete arrangement of resonant elements, which provide ideal platforms for investigating the role of topological optical states in thermal radiation transport in the framework of many-body radiative heat transfer [36–40]. In particular, previous studies have revealed that the topological phonon polaritons (TPhPs) can considerably enhance near-field radiative heat transfer (NFRHT) between nanoparticles (NPs) as they may provide extra channels for NFRHT. Biehs and coworkers [41] investigated radiative heat transfer and the scaling law between the two ends of topologically trivial and nontrivial Su-Schrieffer-Heeger (SSH) chains composed of plasmonic InSb spherical NPs, they presented a dominant contribution of the edge states in a topologically nontrivial SSH chain. Two of the authors [42] proposed SiC NPs chains mimicking the Aubry-André-Harper (AAH) model, which also exhibit an enhancement in NFRHT in those chains with topologically nontrivial configuration, and a semi-analytical explanation was presented. However, except for a few studies which paid their attention to topological optical states in 2D or quasi-2D many-particle radiative heat transfer systems [42–45], most of the previous studies have focus on NFRHT in 1D systems [41,46–53]. More importantly, a thorough investigation of the effects of high-order optical states on radiative heat transfer, including how the long- and short-range dipole-dipole interactions as well as the boundaries can affect the radiative transport, is still lacking.

In this work, we propose subwavelength lattices composed of identical SiC NPs which support phonon polaritons to mimic the 2D SSH model. By employing the coupled dipole approach, which takes into account the long-range dipole-dipole interactions and retardation effects in the NP arrays, we obtain the band structures of the lattices under periodic boundary conditions (PBCs). The topological properties of the lattices are then characterized by the 2D Zak phases of their energy bands, and the numerical results indicate that the lattices with certain geometrical parameters have nonzero 2D Zak phases as expected in electronic systems, which can be recognized as topologically nontrivial. We confirm the existence of high-order TPhPs under open boundary conditions (OBCs), which is consistent with the principle of bulk-edge-corner correspondence. The radiative heat transfer spectra between NPs are calculated based on the many-body radiative heat transfer theory. We show that the power spectra of the topologically nontrivial lattices are appreciably modulated comparing to that of topologically trivial lattices due to the existence of TPhPs. To further reveal the roles that TPhPs play in NFRHT, three kinds of interfaces are constructed, and the contributions of in-plane (IP) mode and out-of-plane (OP) are discussed separately. The numerical results indicate that the high-order TPhPs play dominant roles in radiative heat transfer between the corner NPs while the edge states have negligible impact on it. Moreover, we find that the TPhPs show a moderate robustness against perturbation by introducing random disorder and defects in the lattice. Our study provides a comprehensive understanding on the NFRHT in many-particle systems with high-order topological properties and hence a new approach to modulate NFRHT on the perspective of high-order topology.

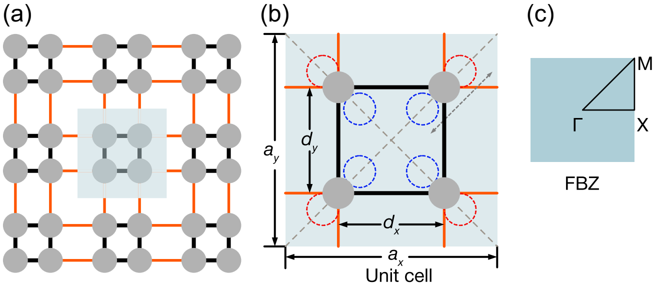

FIG. 1. (a) Schematic of the lattice structure, (b) the unit cell and geometrical parameters, (c) high symmetry points in the first Brillouin zone.

II. MODEL

The 1D SSH model is abstracted from the electron hopping in polyacetylene [54], which can be considered as a dimerized chain, and the relative strength between inter- and intracell hopping determines the topological properties of the chain. The 2D SSH model is an extension of the 1D SSH model, which can be constructed by SSH chains in two orthogonal directions. In this paper, we consider 2D arrays composed of identical spherical α-SiC nanoparticles which support strongly localized phonon polariton resonances in the infrared region due to the excitation of transverse optical phonons. All the NPs are confined in xy plane, as shown in Fig. 1(a). To mimic the 2D SSH model, 4 NPs form a unit cell in which the lattice constants in x and y direction are a_x and a_y, as illustrated in Fig. 1(b). The first Brillouin zone (FBZ) of the NP arrays and high symmetry points in FBZ are illustrated in Fig. 1(c). The intracell hopping is denoted by the black solid lines, while the intercell hopping is denoted by the red solid lines. The hopping strength is regulated by the interparticle distances in both x and y direction, which can be recognized as dimerization in the 2D SSH model. Note that in addition to the nearest-neighbor hopping, which is generally considered in the conventional 2D SSH model, here we also take into account the long-range interactions between the NPs in the array.

We define $\beta_i = d_i/a_i, i = x, y$ to describe the degree of dimerization, the other parameters are set as $a_x = a_y = 0.1\lambda_0$, in which λ_0 is the resonance wavelength of a single SiC NP and the radii of the NPs are 78 nm. In this paper, we limit our discussion under the condition that the degree of dimerization is the same along x and y directions, i.e., $\beta_x = \beta_y = \beta$.

A. Derivation of the eigenfrequencies and eigenstates

The SiC NPs with radii R in the 2D array are located at points $\mathbf{r}_i = (x_i, y_i, z_i),\ i = 1, 2, 3, \ldots, N$. The permittivity of SiC can be described by the Lorentz model as [55]

$$\varepsilon_{\mathrm{p}}(\omega) = \varepsilon_\infty\left(1 + \frac{\omega_{\mathrm{L}}^2 - \omega_{\mathrm{T}}^2}{\omega_{\mathrm{T}} - \omega^2 - \mathrm{i}\omega\gamma}\right), \tag{1}$$

in which ω is the angular frequency of the driving electric field, $\varepsilon_\infty = 6.7$ is the high-frequency limit of permittivity, $\omega_{\mathrm{T}} = 790\ \mathrm{cm}^{-1}$ is the angular frequency of transverse optical phonons (cm^{-1} is used as the unit of angular frequencies for brevity), $\omega_{\mathrm{L}} = 966\ \mathrm{cm}^{-1}$ is the angular frequency of longitudinal optical phonons and $\gamma = 5\ \mathrm{cm}^{-1}$ is the nonradiative damping coefficient (decay rate or linewidth) [55]. The electrical response of each NP can be characterized by its polarizability and can be expressed as [56]

$$\alpha = \frac{4\pi R^3\alpha_0}{1 - 2\mathrm{i}\alpha_0(k_0R)^3/3}, \tag{2}$$

where $k_0 = \omega/c$ denotes the norm of the free-space wave vector and $\alpha_0 = (\varepsilon_\mathrm{p} - 1)/(\varepsilon_\mathrm{p} + 2)$. By substituting Eq. (1) into Eq. (2), the resonance frequency of a single SiC NP can be obtained, i.e., $\omega_\mathrm{res} = 928.5\ \mathrm{cm}^{-1}$.

When the distance between the centers of the nearest NPs is greater than $3R$, each NP can be approximately treated as an electric dipole [57]. The electric response of the entire NP array can be calculated by a set of coupled equations which relate the incident electric field and the electric dipoles [58,59], i.e.,

$$\mathbf{p}_j(\omega) = \alpha(\omega)\mathbf{E}_\mathrm{inc}(\omega, \mathbf{r}_j) + \alpha(\omega)\frac{\omega^2}{c^2}\sum_{i=1,i\neq j}^{N}\hat{\mathbf{G}}_0(\omega, \mathbf{r}_j, \mathbf{r}_i)\mathbf{p}_i(\omega), \tag{3}$$

where $\mathbf{p}_j$ is the excited electric dipole moment of jth NP, $\mathbf{E}_\mathrm{inc}$ is the incident external electric field and $\hat{\mathbf{G}}_0(\omega, \mathbf{r}_j, \mathbf{r}_i)$ is the free-space Green's tensor which describes the propagation of field emitted from ith NP to jth NP. The electric-electric Green's function (GF) takes the form [60]

$$\begin{aligned}\hat{\mathbf{G}}_{0,ij} :&= \hat{\mathbf{G}}_0(\omega, \mathbf{r}_j, \mathbf{r}_i)\\ &= \frac{e^{\mathrm{i}k_0r_{ij}}}{4\pi r_{ij}}\left[\left(1 + \frac{\mathrm{i}}{k_0r_{ij}} - \frac{1}{k_0^2{r_{ij}}^2}\right)\mathbf{I}\right.\\ &\quad\left. + \left(-1 - \frac{3\mathrm{i}}{k_0r_{ij}} + \frac{3}{k_0^2r_{ij}^2}\right)\frac{\mathbf{r}_{ij}\otimes\mathbf{r}_{ij}}{r_{ij}^2}\right],\end{aligned} \tag{4}$$

where $r_{ij} = |\mathbf{r}_i - \mathbf{r}_j|$ is the distance between jth and ith NP. In this scenario, we take both the near-field and the far-field dipole-dipole interactions into account, which is beyond the nearest-neighbor approximation [61] or next-nearest-neighbor approximation [62] in conventional SSH models in electronic system.

According to the polarization directions of the dipoles, we decompose the modes into OP part and IP part. Since all the NP lies in the xy plane, GF can be decomposed into the z part (OP) and the xy part (IP), respectively. For OP mode, GF degenerates to a scalar and can be expressed as

$$\hat{G}^z_{0,ij} = \frac{e^{\mathrm{i}k_0r_{ij}}}{4\pi r_{ij}}\left[\left(1 + \frac{\mathrm{i}}{k_0r_{ij}} - \frac{1}{k_0^2r_{ij}^2}\right)\right]. \tag{5}$$

For IP mode, GF degenerates to a 2×2 tensor which can be expressed as

$$\begin{aligned}\hat{\mathbf{G}}^{xy}_{0,ij} &= \frac{e^{\mathrm{i}k_0r_{ij}}}{4\pi r_{ij}}\left[\left(1 + \frac{\mathrm{i}}{k_0r_{ij}} - \frac{1}{k_0^2{r_{ij}}^2}\right)\mathbf{I}\right.\\ &\quad\left. + \left(-1 - \frac{3\mathrm{i}}{k_0r_{ij}} + \frac{3}{k_0^2{r^2}_{ij}}\right)\frac{\hat{\rho}_{ij}\otimes\hat{\rho}_{ij}}{|\hat{\rho}_{ij}|^2}\right],\end{aligned} \tag{6}$$

here $\hat{\rho}$ is a two-dimensional vector satisfying $\hat{\mathbf{r}}_{ij} = \hat{\rho}_{ij} + (z_i - z_j)\hat{\mathbf{z}}$.

Consider

$$\mathbf{G_0} = \begin{bmatrix} \mathbf{0} & \widehat{\mathbf{G}}_{0,12} & \cdots & \widehat{\mathbf{G}}_{0,1N} \\ \widehat{\mathbf{G}}_{0,21} & \mathbf{0} & \cdots & \widehat{\mathbf{G}}_{0,2N} \\ \vdots & \vdots & \ddots & \vdots \\ \hat{\mathbf{G}}_{0,N1} & \hat{\mathbf{G}}_{0,N2} & \cdots & \mathbf{0} \end{bmatrix} \tag{7}$$

as the interaction matrix and $|\mathbf{P}\rangle = [\mathbf{p}_1, \mathbf{p}_2, \mathbf{p}_3, \ldots, \mathbf{p}_N]^\mathrm{T}$ as the dipole moment distribution, $|\mathbf{E}\rangle = [\mathbf{E}_{\mathrm{inc},1}, \mathbf{E}_{\mathrm{inc},2}, \ldots, \mathbf{E}_{\mathrm{inc},N}]^\mathrm{T}$ as the incident electric field vector. The coupled-dipole equations can be written in a more compact form, i.e.,

$$|\mathbf{P}\rangle = \alpha\big[|\mathbf{E}\rangle + k_0^2\mathbf{G}_0\cdot|\mathbf{P}\rangle\big]. \tag{8}$$

For the finite NP arrays, the eigenstates can be determined by setting the incident field to be zeros. And the equation is then simplified to an eigenvalue problem:

$$k_0^2\mathbf{G_0}|\mathbf{P}\rangle = \alpha^{-1}(\omega)|\mathbf{P}\rangle. \tag{9}$$

By solving the above equation, a series of complex eigenvalues can be obtained as $\omega_i = \widetilde{\omega}_i - \mathrm{i}\Gamma_i/2$, in which $\widetilde{\omega}_i$ is the eigenfrequency and Γ_i is the decay rate of ith state. The corresponding eigenvector is the dipole moment distribution of the state.

Notice that the topological protected eigenstates are highly localized over the interfaces between topologically trivial and nontrivial regions, we use the inverse participation ratio (IPR) [47,63–65] to recognize these states and the IPR of a state is defined as

$$\mathrm{IPR} = \frac{\sum_{i=1}^{N}|\mathbf{p}_i|^4}{(\sum i = 1^N|\mathbf{p}_i|^2)^2}. \tag{10}$$

The dipole moment distribution of an eigenstate with IPR $= 1/M$ (M is a positive integer) can be equivalently regarded as evenly distributed over M NPs [63]. Therefore, for a highly localized topologically nontrivial state, its IPR will be much larger than a bulk one.

To obtain the eigenstates and dipole moment distributions for 2D arrays under PBCs, we apply Bloch theorem to Eq. (8), and the dipole moment distribution takes the form

$$|\mathbf{P}\rangle = [\ldots, \mathbf{p}_{(m,n,1)}, \mathbf{p}_{(m,n,2)}, \mathbf{p}_{(m,n,3)}, \mathbf{p}_{(m,n,4)}, \ldots]^\mathrm{T},\ m, n \in \mathbb{Z}. \tag{11}$$

where $\mathbf{p}_{(m,n,i)}$ is the dipole moment of the ith NP of (m, n)th cell. According to the Bloch theorem,

$$\mathbf{p}_{(m,n,i)} = e^{\mathbf{i}\mathbf{R}_\mathrm{mn}\cdot(\mathbf{k}+\mathbf{K})}\mathbf{p}_i,\ i = 1, 2, 3, 4,\ \text{and}\ m, n \in \mathbb{Z}, \tag{12}$$

where $\mathbf{R}_{mn} = m \cdot \mathbf{a}_x + n \cdot \mathbf{a}_y$ denotes the position vector of (m, n)th unit cell, $\mathbf{k}$ is the Bloch wave vector in the FBZ and $\mathbf{K}$ is the reciprocal lattice vector. The coupled dipole equation can be expressed in terms of the Bloch part of the dipole moment ($|\mathbf{P_k}\rangle = [\mathbf{p}_1,\ \mathbf{p}_2,\ \mathbf{p}_3,\ \mathbf{p}_4]^{\mathrm{T}}$)

$$k_0^2 \mathbf{G_k}\,|\mathbf{P_k}\rangle = \alpha^{-1}(\omega)|\mathbf{P_k}\rangle, \tag{13}$$

where

$$\mathbf{G}_{\mathrm{k}} = \begin{bmatrix} \hat{\mathbf{G}}_{\mathrm{k},11} & \hat{\mathbf{G}}_{\mathrm{k}12} & \hat{\mathbf{G}}_{\mathrm{k},13} & \hat{\mathbf{G}}_{\mathrm{k},14} \\ \hat{\mathbf{G}}_{\mathrm{k},21} & \hat{\mathbf{G}}_{\mathrm{k},22} & \hat{\mathbf{G}}_{\mathrm{k},23} & \hat{\mathbf{G}}_{\mathrm{k},24} \\ \hat{\mathbf{G}}_{\mathrm{k},31} & \hat{\mathbf{G}}_{\mathrm{k},32} & \hat{\mathbf{G}}_{\mathrm{k},33} & \hat{\mathbf{G}}_{\mathrm{k},34} \\ \hat{\mathbf{G}}_{\mathrm{k},41} & \hat{\mathbf{G}}_{\mathrm{k},42} & \hat{\mathbf{G}}_{\mathrm{k},43} & \hat{\mathbf{G}}_{\mathrm{k},44} \end{bmatrix} \tag{14}$$

is the GF of the entire lattice under PBC. The diagonal terms in $\mathbf{G}_{\mathrm{k}}$ can be calculated as

$$\begin{aligned}\widehat{\mathbf{G}}_{\mathbf{k},ii}(\omega) &= \sum_{\substack{m,n\in\mathbb{Z},\\ \mathbf{R}_{mn}\neq 0}} \widehat{\mathbf{G}}_0(\omega,\mathbf{R}_{mn},\mathbf{0})\mathrm{e}^{\mathrm{i}\mathbf{k}\cdot\mathbf{R}_{mn}} \\ &= \sum_{\substack{m,n\in\mathbb{Z},\\ \mathbf{R}_{mn}\neq 0}} \frac{\mathrm{e}^{\mathrm{i}k_0R_{mn}+\mathrm{i}\mathbf{k}\cdot\mathbf{R}_{mn}}}{4\pi R_{mn}}\left[\left(1+\frac{\mathrm{i}}{k_0R_{mn}}-\frac{1}{k_0^2R_{mn}^2}\right)\mathbf{I}\right. \\ &\quad \left. +\left(-1-\frac{3\mathrm{i}}{k_0R_{mn}}+\frac{3}{k_0^2R_{mn}^2}\right)\frac{\mathbf{R}_{mn}\otimes\mathbf{R}_{mn}}{R_{mn}^2}\right],\end{aligned} \tag{15}$$

and the off-diagonal terms can be expressed as

$$\begin{aligned}\widehat{\mathbf{G}}_{\mathbf{k},ij}(\omega) &= \sum_{m,n\in\mathbb{Z}} \widehat{\mathbf{G}}_0(\omega,\mathbf{R}_{mn},\mathbf{s}_{ij})\mathrm{e}^{\mathrm{i}\mathbf{k}\cdot\mathbf{R}_{mn}} = \sum_{m,n\in\mathbb{Z}} \widehat{\mathbf{G}}_0\big(\omega,\mathbf{S}_{mn}^{ij},\mathbf{0}\big)\mathrm{e}^{\mathrm{i}\mathbf{k}\cdot\mathbf{R}_{mn}}\ \big(\text{let } \mathbf{S}_{mn}^{ij} = \mathbf{R}_{mn}-\mathbf{s}_{ij}\big) \\ &= \sum_{m,n\in\mathbb{Z}} \frac{\mathrm{e}^{\mathrm{i}k_0S_{mn}^{ij}+\mathrm{i}\mathbf{k}\cdot\mathbf{R}_{mn}}}{4\pi S_{mn}^{ij}}\left[\left(1+\frac{\mathrm{i}}{k_0S_{mn}^{ij}}-\frac{1}{\big(k_0S_{mn}^{ij}\big)^2}\right)\mathbf{I}+\left(-1-\frac{3\mathrm{i}}{k_0S_{mn}^{ij}}+\frac{3}{\big(k_0S_{mn}^{ij}\big)^2}\right)\frac{\mathbf{S}_{mn}^{ij}\otimes\mathbf{S}_{mn}^{ij}}{(S_{mn}^{ij})^2}\right],\end{aligned} \tag{16}$$

where $\{i,\ j\}_{i\neq j} \in \{1, 2, 3, 4\}$ and $\mathbf{s}_{ij}$ is the position vector from ith NP to jth NP in a unit cell.

The eigenfrequencies and corresponding dipole moment distributions of periodic NP array can be obtained by solving the eigenvalue problem in Eq. (13). The $1/r$ term in the series makes the GF converges slowly in real space, hence, we apply Poisson's summation and Ewald's summation method to achieve a faster convergence, detailed derivation can be found in Appendix B and also in Ref. [35].

B. Band topology

We plot the IP mode and OP mode band structures of 2D SSH NP arrays under PBCs with $\beta = 0.25\,(0.75)$ and 0.5 respectively in Fig. 2, where the color indicates the normalized imaginary parts of the eigenstates via $(\Gamma_i - \gamma)/\gamma$. As can be

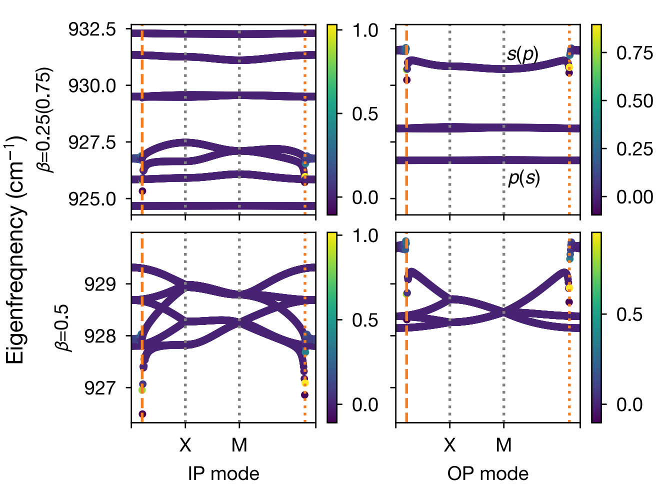

FIG. 2. The IP mode (left column) and OP mode (right column) band structures under $\beta = 0.25$, 0.5, and 0.75.

seen in the figure, the 2D SSH lattices with $\beta = 0.75$ and $\beta = 0.25$ share the same band structure, since their geometrical structures are exactly the same. For both the IP mode and OP mode band structures, their energy bands are divergent near the light line (the dash lines in the subfigures) due to the strong coupling with free-space radiation from the long-range dipole-dipole interaction as well as the retardation effect. For the lattice under $\beta = 1/2$, the primitive cell contains only 1 NP, which results in the double and quadrupole degenerate states at high symmetry points. Eight and four bands are observed in IP mode and OP mode band structures respectively, this is because the NPs can be polarized along x and y directions in IP mode while can only be polarized along z direction in OP mode. Besides, since the stronger near-range dipole-dipole interaction in IP mode, the eigenfrequencies cover a wider range than that of OP mode, and the discontinuity of energy bands near light line is not that obvious as in OP mode for the lack of $1/r$ term. It is worth mentioning that the nonconvergence in both the IP mode and OP mode band structures is obtained from rigorous calculation, which is generally ignored by many of the derivations [41,66,67].

The 2D Zak phase ($\theta_i,\ i = x, y$) can be used to reveal the topological properties of the 2D SSH model [35,61,68,69]. The topological edge states are expected to emerge in the lattices under OBCs when any of θ_x or θ_y is nonzero. Furthermore, when a lattice features both nonzero θ_x and nonzero θ_y, the corner states are expected to emerge in the lattice under OBC. In this paper, the 2D Zak phase is numerically obtained by means of Wilson loop (see details in Appendix A). We can clearly observe that the Zak phase for the first and third gap in OP mode is quantized as a function of β_x and β_y, and can be expressed as:

$$\theta_i = \begin{cases} 0, & 3R/a_i \leqslant \beta_i < 1/2 \\ 1, & 1/2 < \beta_i \leqslant 1 - 3R/a_i \end{cases} \text{for } i = x, y, \tag{17}$$

which is consistent as in the electron system considering nearest-neighbor interaction. Hence, we can conclude that the topological behaviors in the conventional 2D SSH model are still valid in the photonic system composed of SiC NPs with the consideration of long-range interactions.

Parities of lattices with $\beta = 0.25(0.75)$ and $\beta = 0.5$ are marked in Fig. 2, the two lattices share the same band structure while opposite parities at X point in the FBZ. In the meanwhile, during the variation of β from 0.25 to 0.5 and then 0.75, the band gap between the 3rd and 4th band is firstly closed at Dirac point and then reopened, which indicates a topological phase transition from trivial phase to nontrivial phase [26,70].

C. Calculation of heat transfer rate

Within the dipole approximation, the radiative heat transfer rate between the NPs can be calculated based on fluctuation-dissipation theorem (FDT) in the theoretical framework of many-body radiative heat transfer theory [36–38,71–75]. The coupled dipole model with fluctuating dipoles due to thermal excitation can be expressed as [36]

$$|\mathbf{E}\rangle = \mu_0\omega^2\mathbf{G_0}|\mathbf{P}^{\mathrm{fl}}\rangle + k_0^2\mathbf{G_0}|\alpha\mathbf{E}\rangle, \tag{18}$$

in which $|\mathbf{P}^{\mathrm{fl}}\rangle$ is the fluctuating dipole moment. The physical significance of the first term in the RHS of Eq. (18) is the direct propagation of the dipole field from the source and the second term indicates the scattering processes from the other NPs due to the exciting electrical fields. The propagation of electromagnetic waves can be considered from the fluctuating dipole by the total GF $\mathbf{G}$ which includes the many-body scattering processes, which reads

$$|\mathbf{E}\rangle = k_0^2\mathbf{G}|\mathbf{P}^{\mathrm{fl}}\rangle = k_0^2\big(\mathbf{I} - \alpha k_0^2\mathbf{G}_0\big)^{-1}\mathbf{G}_0|\mathbf{P}^{\mathrm{fl}}\rangle. \tag{19}$$

The total GF can be written as

$$\mathbf{G} = \big(\mathbf{I} - \alpha\, k_0^2\mathbf{G}_0\big)^{-1}\mathbf{G}_0 = \begin{bmatrix} \widehat{\mathbf{0}} & \widehat{\mathbf{G}}_{12} & \dots & \widehat{\mathbf{G}}_{1N} \\ \widehat{\mathbf{G}}_{21} & \widehat{\mathbf{0}} & \dots & \widehat{\mathbf{G}}_{2N} \\ \vdots & \vdots & \ddots & \vdots \\ \widehat{\mathbf{G}}_{N1} & \widehat{\mathbf{G}}_{N2} & \dots & \widehat{\mathbf{0}} \end{bmatrix}, \tag{20}$$

where $\widehat{\mathbf{G}}_{ij},\ i \neq j$ is the 3×3 composing matrix block of the total GF.

By using FDT, the heat transfer rate from jth NP to ith NP is given by

$$\mathcal{P}_{j\rightarrow i} = 3\int_0^\infty \frac{d\omega}{2\pi}\Theta(\omega, T_j)\mathcal{T}_{i,j}(\omega), \tag{21}$$

in which $\Theta(\omega, T_j) = \frac{\hbar\omega}{\exp(\hbar\omega/k_bT)-1}$ is the energy of Planck oscillator with $\hbar$ and k_b being the Planck constant and Boltzmann constant respectively, and the transmission coefficient (TC) is defined as:

$$\mathcal{T}_{i,j}(\omega) = \frac{4}{3}\Big(\frac{\omega}{c}\Big)^4\chi_i\chi_j\mathrm{Tr}(\widehat{\mathbf{G}}_{ij}\widehat{\mathbf{G}}_{ij}^{\dagger}), \tag{22}$$

where $\chi_i = \mathrm{Im}(\alpha_i) - \frac{k_0^3|\alpha_i|^2}{6\pi}$ is the susceptibility of the isotropic NPs [72]. Since all the NPs are confined in xy plane, the nonzero elements in $\widehat{\mathbf{G}}_{ij}$ can be decomposed into the xy and z parts:

$$\widehat{\mathbf{G}}_{ij} = \begin{bmatrix} \widehat{\mathbf{G}}_{ij}^{xy} & \widehat{\mathbf{0}}_{2\times 1} \\ \widehat{\mathbf{0}}_{1\times 2} & \widehat{G}_{ij}^{z} \end{bmatrix} \tag{23}$$

and the total radiative heat transfer can be recognized as the sum of radiative heat transfer through IP mode and OP mode. The corresponding TC is given by

$$\begin{aligned} \mathcal{T}_{i,j}^{\mathrm{IP}}(\omega) &= \frac{4}{3}\frac{\omega^4}{c^4}\chi_i\chi_j\mathrm{Tr}\big(\widehat{\mathbf{G}}_{ij}^{xy}\widehat{\mathbf{G}}_{ij}^{\dagger,xy}\big), \\ \mathcal{T}_{i,j}^{\mathrm{OP}}(\omega) &= \frac{4}{3}\frac{\omega^4}{c^4}\chi_i\chi_j\mathrm{Tr}\big(\widehat{G}_{ij}^{z}\widehat{G}_{ij}^{\dagger,z}\big). \end{aligned} \tag{24}$$

III. FINITE 2D SSH LATTICES

According to Eq. (17), the 2D Zak phase is (π, π) for lattice with $\beta = 0.75$ and (0, 0) for lattice with $\beta = 0.25$ under PBCs, which are considered to be topologically trivial and nontrivial. According to the bulk-edge-corner correspondence, the topological edge and corner states (TPhPs and high-order TPhPs) are expected to emerge at the interface between topologically nontrivial and topologically trivial region when applying OBCs to the lattices.

To study the effects of 2D Zak phases on the eigenstates (dipole moment distributions) of the 2D SSH lattices under OBCs, we construct finite 2D NP arrays with topologically trivial and nontrivial properties in this section. The nontrivial region can be realized by setting $\beta = 0.75$ in the finite 2D SSH lattice. For the construction of trivial region, we have two approaches, i.e., the vacuum whose 2D phase is naturally zero and the 2D SSH lattice with $\beta = 0.25$. To study the influence of these two kinds of trivial regions on eigenstate spectra and radiative heat transfer, we consider the following three cases, illustrated in Fig. 3, on the basis of the finite 2D SSH lattice with $\beta_0 = 0.75$: the individual 2D SSH lattice surrounded by vacuum (Case I), the joint lattice which is constructed through connecting one side of the original lattice to another 2D SSH lattice whose $\beta = 0.25$ (case II), and the joint lattice which is constructed through surrounding the original lattice with another 2D SSH lattice whose $\beta = 0.25$ and forming a larger nested square lattice (case III). In this paper, we call the configurations of the lattices in these three cases "topologically nontrivial," and the configurations "topologically trivial" after we substitute the nontrivial region in these cases with finite lattice whose $\beta = 0.25$. Without causing ambiguity, we will simply refer to them as nontrivial lattices and trivial lattices respectively in the following discussion. NPs in the 4 corners of the original finite 2D SSH lattice are labeled as NP A, B, C, and D, as illustrated in Fig. 3.

A. Case I

Firstly, we focus on an individual finite lattice in vacuum (the case I illustrated in Fig. 3). Since the 2D Zak phase of the topologically nontrivial lattice is (π, π), the localized edge states are expected to emerge in both x and y direction according to the bulk-edge correspondence. Furthermore, this set of Zak phase also implies the existence of high-order corner states according to the bluk-edge-corner correspondence [35].

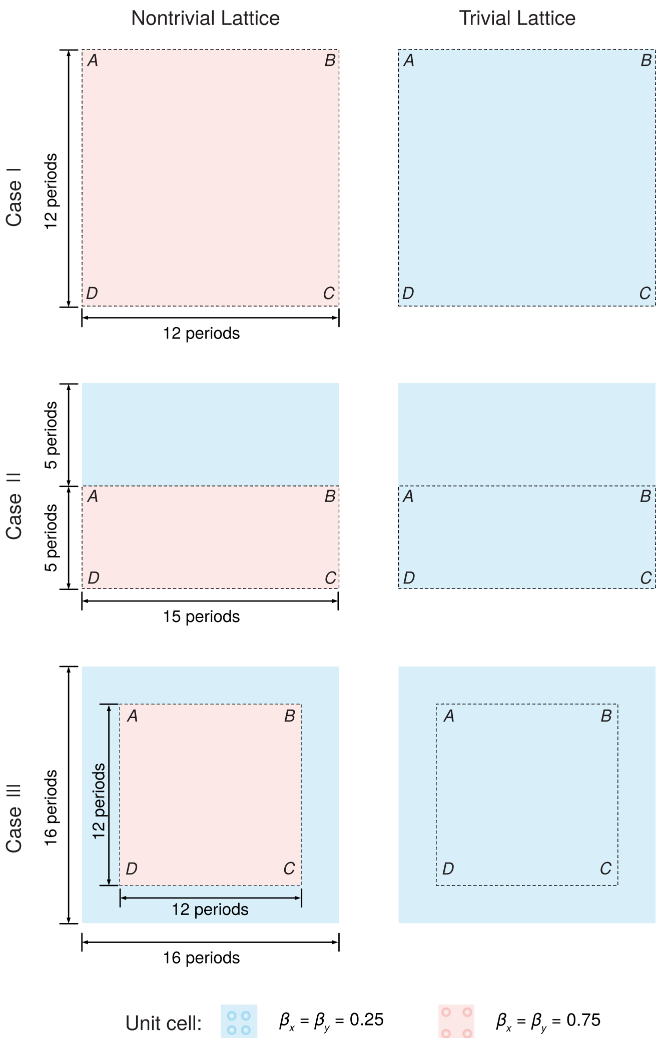

FIG. 3. Geometrical configuration of the three cases, lattices in the left column have topologically nontrivial configurations, while in the right column have trivial configurations.

The IP mode and OP mode eigenstate spectra of the topologically nontrivial lattice are illustrated in Figs. 4(a) and 4(b), respectively, in which the states are sorted in ascending order according to the real part of the eigenfrequencies and the color stands for the IPR of each eigenstates. The eigenstate spectra of the corresponding topologically trivial lattice are calculated and shown in Figs. 4(c) and 4(d). It can be seen in the figure that the band structures of the topologically nontrivial and trivial lattice are very similar, the band gaps both appear in similar frequency ranges and the main gaps of the two lattices appear at around the single-particle resonance frequency (927.7–929.3 cm^{-1}), which is due to the fact that these two lattices share the same band structure under PBC. However, in Figs. 4(a) and 4(b), states with high IPR (0.35 and 0.25) can be clearly recognized in the main gap of the nontrivial lattice, which is different from the trivial lattice. We plot the dipole moment distribution of these states in Figs. 4(e) and 4(f). In Fig. 4(e), the IPR of the 575th state is 0.35 and the dipole moment distribution is localized in the NPs at diagonal corners. In Fig. 4(f), the dipole moment distribution is evenly localized over the four corners in the nontrivial lattice, as the IPR of this state ($\sim 1/4$) implies. Besides, the nontrivial lattice also supports topological edge states stemming from the bulk-edge correspondence. In Figs. 4(g) and 4(h), we also plot the dipole moment distribution of the edge states which have relatively higher IPRs than the bulk states. The dipole moment distribution of the edge states show localized behaviors either over the opposite two sides or the four sides of the square lattice. We also note that for the edge states, the dipole moments tend to distribute mostly over the centers of the sides and decay along the edge, resulting the dipole moments of the corner NPs are comparable to that of bulk NPs.

The spectral net heat transfer rate between NP A and NP C ($p^{\nu}_{\mathrm{net}}(\omega)$, $\nu =$ IP, OP or Total) is shown in Fig. 5. We assume that the temperature of NP A is 310 K, and all the remaining NPs are kept at room temperature, i.e., 300 K. This temperature distribution is chosen to partially match the resonance frequency of the SiC phonon polariton and avoid the radiative heat transfer contribution from the NPs other than NP A. The spectral radiative heat transfer contribution from the IP mode and OP mode are plotted separately in Figs. 5(a) and 5(b), by taking summation of the two parts, the total spectral radiative heat transfer rate is plotted in Fig. 5(c). A pronounced difference in $p^{\nu}_{\mathrm{net}}(\omega)$ can be observed in the figures. For the nontrivial lattice, the spectral radiative heat transfer rates at $\omega = \omega_{\mathrm{res}} = 928.5\ \mathrm{cm}^{-1}$ are $p^{\mathrm{IP}}_{\mathrm{net}}(\omega_{\mathrm{res}}) = 6.46 \times 10^{-20}$ W cm, $p^{\mathrm{OP}}_{\mathrm{net}}(\omega_{\mathrm{res}}) = 8.11 \times 10^{-20}$ W cm, $p^{\mathrm{Total}}_{\mathrm{net}}(\omega_{\mathrm{res}}) = 1.46 \times 10^{-19}$ W cm, which are 1.82, 1.68, and 1.74-fold larger than that of topologically trivial lattice. By integrating over the frequency range, we obtain radiative heat transfer rate (p^{ν}_{net}, $\nu =$ IP, OP, or Total). For the topologically nontrivial lattice, $p^{\mathrm{IP}}_{\mathrm{net}} = 2.91 \times 10^{-17}$ W, $p^{\mathrm{OP}}_{\mathrm{net}} = 3.17 \times 10^{-17}$ W, and $p^{\mathrm{Total}}_{\mathrm{net}} = 6.09 \times 10^{-17}$ W. For the trivial lattice, $p^{\mathrm{IP}}_{\mathrm{net}} = 3.02 \times 10^{-17}$ W, $p^{\mathrm{OP}}_{\mathrm{net}} = 2.53 \times 10^{-17}$ W, and $p^{\mathrm{Total}}_{\mathrm{net}} = 5.55 \times 10^{-17}$ W. Here we define the modulation ration, R_{mod}, to characterize the degree of enhancement, which can be expressed as

$$R_{\mathrm{mod}} = \frac{\int d\omega\, p^{\nu}_{\mathrm{net,Nontrivial}}(\omega)}{\int d\omega\, p^{\nu}_{\mathrm{net,Trivial}}(\omega)} \quad \nu = \mathrm{IP,\ OP,\ or\ Total} \tag{25}$$

and R_{mod} for IP, OP, and Total are 0.96, 1.26, and 1.10. The ration of modulation tells that the net radiative heat power from NP A to NP B in nontrivial lattice is suppressed in IP mode and enhanced in OP mode compare to the trivial lattice.

We also notice the differences in peak frequencies of the heat transfer spectra between the trivial lattice and nontrivial lattices. For the nontrivial lattice, the peak values in the power spectra appear at 928.54 and 928.38 cm^{-1} for IP and OP modes, which is close to ω_{res} as well as the eigenfrequencies of the topological corner states, indicating a dominant contribution of the TPhPs supported by the nontrivial lattice. For the trivial lattice, the peak value of $p^{\nu}_{\mathrm{net}}(\omega)$ appears at 926.17 and 929.42 cm^{-1} for IP and OP modes. The result shows that radiative heat transfer is mainly contributed by the bulk states below the main gap in IP mode, while by the bulk states above the main gap in OP mode. This is even clearer by assumming a low-loss circumstance of $\gamma = 1\ \mathrm{cm}^{-1}$ for the permittivity of SiC with other parameters unchanged to avoid the mixed exciting. In Figs. 5(d)–5(f), we plot the spectral radiative heat transfer rates between NP A and NP C under $\gamma = 1\ \mathrm{cm}^{-1}$.

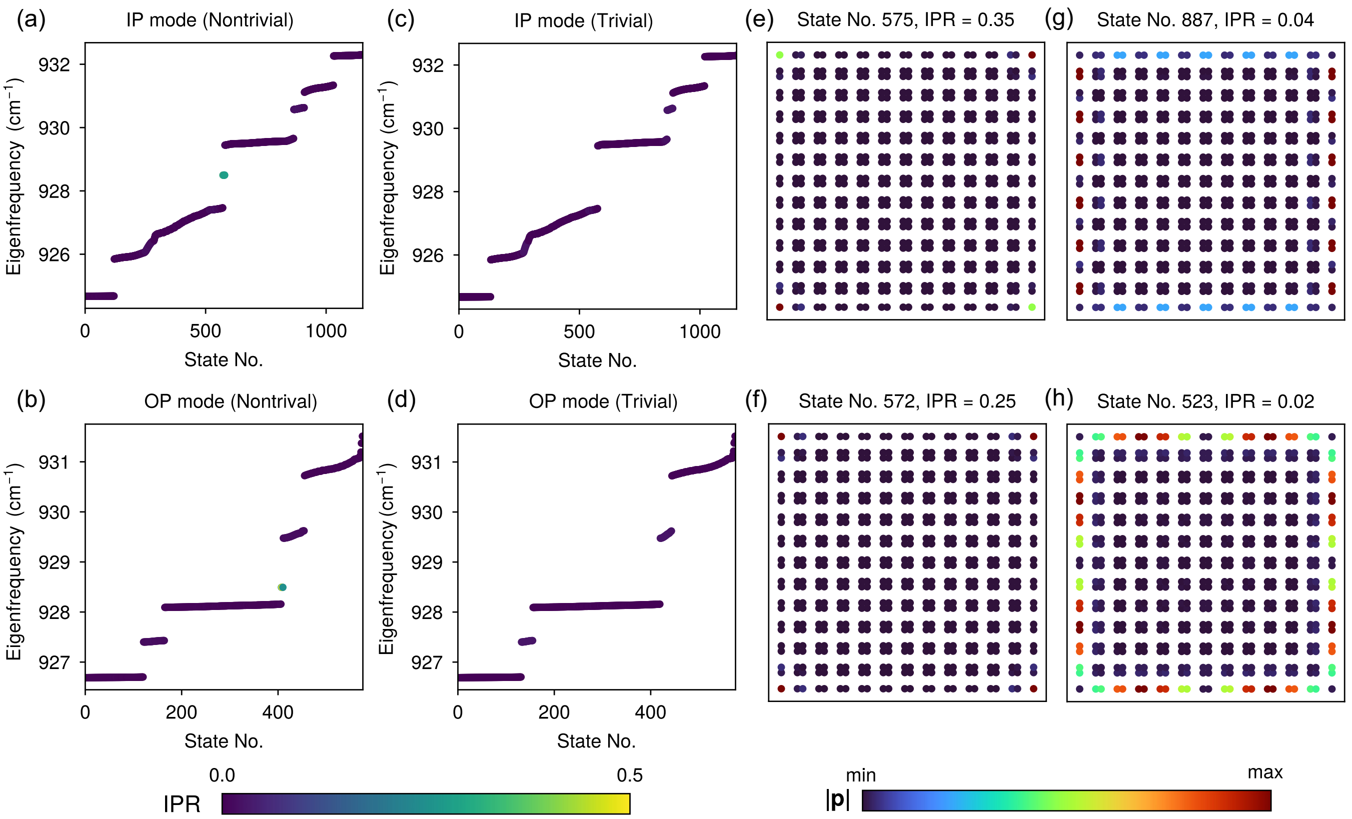

FIG. 4. Band structures and dipole moment distributions of square lattices (case I). (a) the IP mode band structure and (b) the OP mode band structure of the topologically nontrivial lattice, (c) the IP mode band structure and (d) the OP mode band structure of the topologically trivial lattice. The dipole moment distributions of corner states [(e) and (f)] and edge states in IP mode [(g) and (h)].

In this scenario, the dominant states are clearly recognized. Comparing to the condition of $\gamma = 5\ \mathrm{cm}^{-1}$, the net radiative heat transfer powers are enhanced owing to the larger polarizability, detailed discussion can be found in [42]. At the same time, the enhancing effect of TPhPs is more significant, R_{mod} in IP and OP mode are 2.13 and 4.08, respectively, and 3.11 in total.

To further reveal the dominant states of radiative heat transfer in nontrivial and trivial lattices. We focus on the susceptibility term (χ) in $\mathcal{T}_{ij}$, which is strongly dispersive and describes the material response to electrical field in frequency domain. In Fig. 6, we plot the square of χ under the complex eigenfrequencies of the trivial and nontrivial lattices. In Figs. 6(a) and 6(b), χ^2 at eigenfrequencies of corner states are significantly higher than that of bulk states in the nontrivial lattice. This can partially explain why high-order TPhPs can dominate radiative heat transfer in topologically nontrivial lattices [cf. Eq. (24)]. For the trivial lattice, as illustrated in Figs. 6(c) and 6(d), χ^2 at the eigenfrequencies of states below the main gap in IP mode band structure and above the main gap in OP mode have obviously higher values than others, which is responsible for radiative heat transfer in respective states.

To study the modulation effect of the corner/edge states on the radiative heat transfer in the topologically nontrivial lattice. We consider radiative heat transfer between one of the four corner NPs (the lower left corner) and the remaining NPs in the topologically trivial and nontrivial lattices and calculate the corresponding modulation ration (R_{mod}) under $\gamma = 1\ \mathrm{cm}^{-1}$. The results are shown in Fig. 7, in which the markers indicate the NPs in the topologically nontrivial lattice and the colors are mapped from the values of R_{mod}. Note that the values of R_{mod} have been subtracted by 1 from the definition given by Eq. (25) to better distinguish between enhancement or suppression effects. For IP mode, the radiative heat transfer rates between the corner NP and most of the other NPs are suppressed ($R_{\mathrm{mod}} < 0$) except the diagonal corner. While for OP mode, radiative heat transfer between corner NP and other NPs in the diagonal corner and the edge are enhanced ($R_{\mathrm{mod}} > 0$). The results indicate that TPhPs/high-order TPhPs play vital roles in the modulation of radiative heat transfer between the corner NP and edge/corner NPs. Besides, we also note that for both the IP and OP mode, the radiative heat transfer rate is strongly suppressed when the other NP is chosen as the nearest neighbors of the corner NP while strongly enhanced when the other NP is chosen as the next-nearest neighbors, which is caused by the difference in the distances of the NPs in topologically trivial and nontrivial lattice.

B. Case II

In this case, we consider a joint lattice where the upper side of the topologically nontrivial lattice is connected to a topologically trivial one illustrated in Fig. 3. Each part has 15 periods along x direction and 5 periods along y direction.

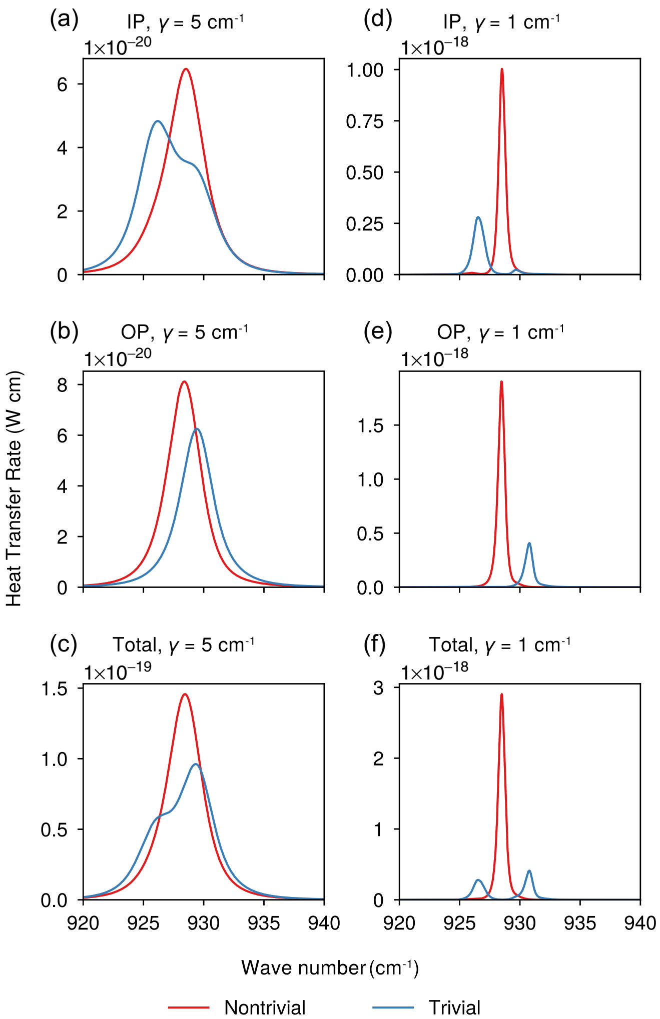

FIG. 5. The radiation heat transfer spectra between NP A and NP C in case I in (a) IP mode and (b) in OP mode, (c) the total power spectrum of the trivial and nontrivial lattice. [(d)–(f)] Net power spectra with decay rate $\gamma = 1\ \mathrm{cm}^{-1}$ in IP mode, OP mode, and total.

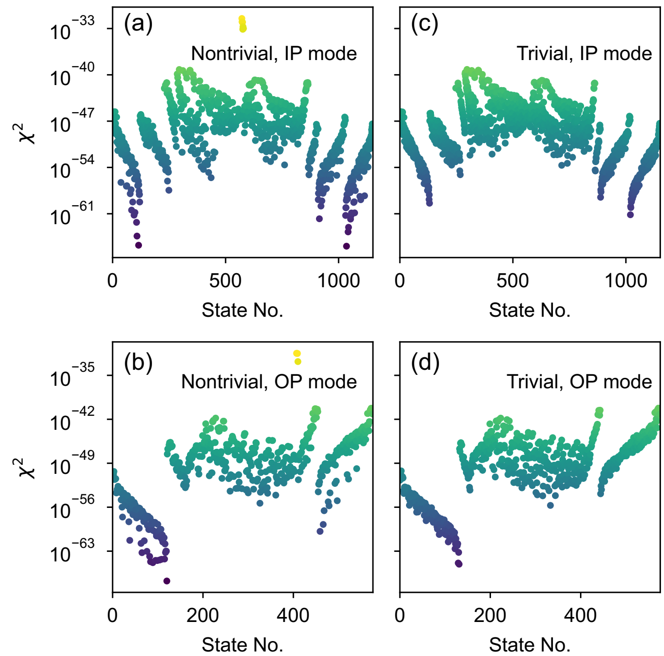

FIG. 6. Susceptibility at complex eigenfrequencies. χ^2 at eigenfrequencies of (a) IP mode and (b) OP mode of topologically nontrivial lattice, as well as (c) IP mode and (d) OP mode of topologically trivial lattice.

For the lattice with nontrivial configuration, the boundaries of the nontrivial region are all topologically trivial with Zak phase being (0, 0). Hence, the topologically protected edge states and corner states are expected to emerge according to the bulk-edge correspondence and edge-corner correspondence. However, since C_{4v} symmetry no longer exists in the lattice while the mirror symmetry is still preserved, the dipole moment distribution should be different from the case I and subsequently affects radiative heat transfer between NPs in the lattice.

The eigenstates spectra of the IP and OP modes of the nontrivial lattice are calculated and shown in Figs. 8(a) and 8(b), in which the colors stand for the IPR of each eigenstates. Figs. 8(c) and 8(d) show the IP mode and OP mode band structures of the trivial lattice. The band structures of the nontrivial and trivial lattices are similar as expected. For the IP mode band structures, the band gaps both appear in similar frequency ranges and the main gap of each lattice appears around ω_{res} (927.6–929.5 cm^{-1}). In Fig. 8(a), states with high IPR ($\sim$1/2) can be clearly recognized in the main gap of the nontrivial lattice, which is different from the band structure of the trivial one. The midgap states with IPR close to 1/2 implies that the dipole moment distribution is localized over 2 NPs in the lattice. It can also be observed in Fig. 8(a) that states with relatively higher IPR appear in the gaps at 926.0 $\mathrm{cm}^{-1} \leqslant \omega \leqslant$ 926.5 cm^{-1} and 929.6 $\mathrm{cm}^{-1} \leqslant \omega \leqslant$ 931.1 cm^{-1}, these states are edge states whose dipole moment distributions are localized over the interface between the topologically nontrivial region and trivial region in the nontrivial side and consistent with the prediction from the bulk-boundary correspondence. Figure 8(e) gives the dipole moment distribution of the 602th state lying in the main gap which has an IPR of 0.47 and is expected to be a localized corner state. The dipole moment is strongly localized over NP A and B and decay rapidly in the surroundings, indicating the existence of high-order topological state. Figure 8(f) gives the dipole moment distribution of the 909th state lying in the gap at 929.6 $\mathrm{cm}^{-1} \leqslant \omega \leqslant$ 931.1 cm^{-1}, the IPR of this state is 0.04, representing an equivalence localization over $\sim$25 nanoparticles. As seen in the figure, the dipole moment demonstrates higher value along the boundaries of the topologically nontrivial region of the nontrivial lattice especially the interface between the trivial and nontrivial region, i.e., the path from NP A to NP B, and hence the state can be recognized as a topological edge state. For comparison, IPR of the 301th state, which is a bulk state, of the nontrivial lattice in Fig. 8(g) is 0.0023 and much lower than that of localized states.

Different from case I, IPRs of all the corner states in case II range from 0.39–0.47. As a consequence, the dipole moment distribution of all these states are localized over two of the corners in the nontrivial region. The lattice sites where the dipole moment distribution is localized are either NP A and

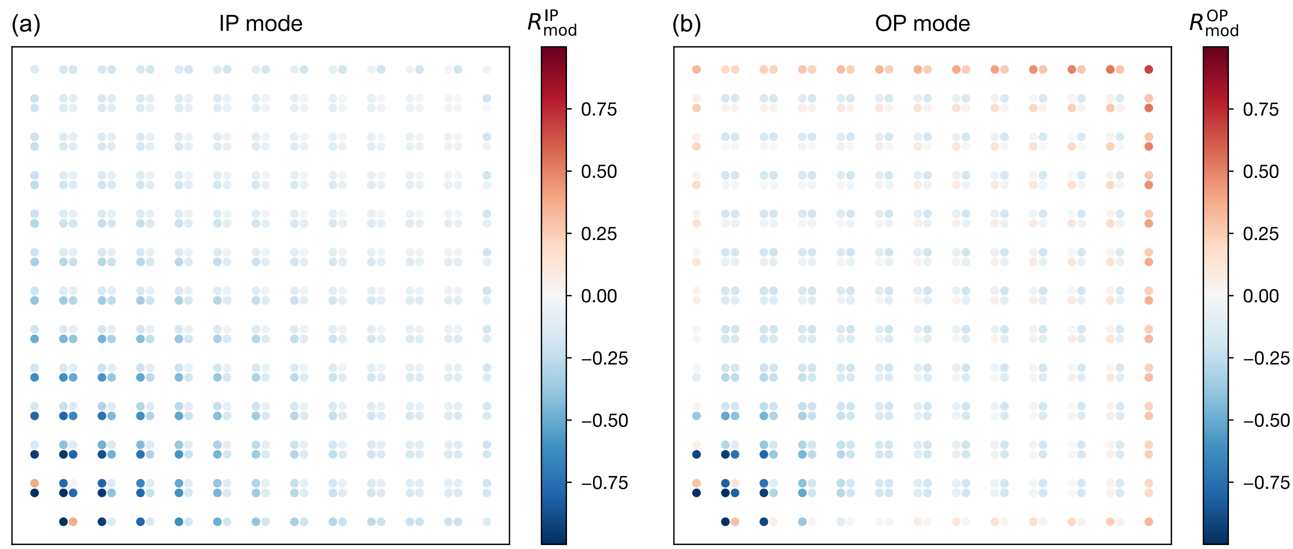

FIG. 7. R_{mod} [subtracting by 1 from the definition given by Eq. (25)] in (a) IP mode and (b) OP mode when one of the NP is fixed at corner while the other is chosen from remaining NPs in the lattice.

NP B or NP C and NP D owing to the breaking of C_{4v} symmetry and the existence of mirror symmetry. Furthermore, the degree of localization, in the perspective of IPR, in case II is also stronger than that in case I, which suggests that the finite 2D SSH lattice with zero Zak phase can better assist in localizing dipole moment to the corner compare to vacuum.

Figure 9 demonstrates the net radiative heat transfer between NP A and NP B in nontrivial and trivial lattice. The temperature of NP A is set to be 310 K and other NPs are set to be 300 K. For the trivial lattice, the spectral radiative heat transfer rates at $\omega_{\mathrm{res}} = 928.5\ \mathrm{cm}^{-1}$ are $p^{\mathrm{IP}}_{\mathrm{net}}(\omega_{\mathrm{res}}) = 1.18 \times 10^{-19}$ W cm and $p^{\mathrm{IP}}_{\mathrm{net}}(\omega_{\mathrm{res}}) = 3.39 \times 10^{-20}$ W cm, respectively. The spectral heat transfer rates at ω_{res} for the

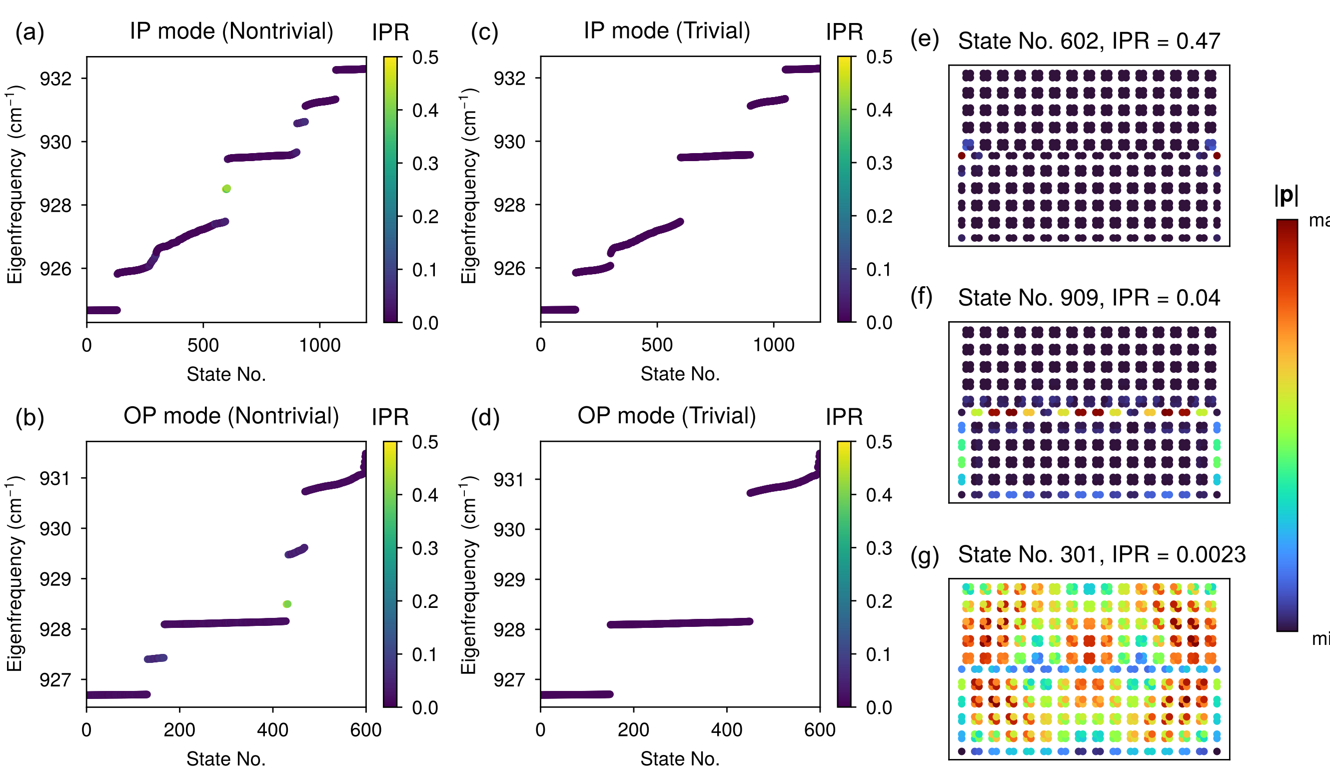

FIG. 8. Band structures and dipole moment distributions of the single side connected lattices (case II). (a) the IP mode band structure and (b) the OP mode band structure of the connected lattice with topologically nontrivial configuration, (c) the IP mode band structure and (d) the OP mode band structure of the connected with topologically trivial configuration. The dipole moment distributions of (e) corner state, (f) edge state, and (g) bulk state in IP mode.

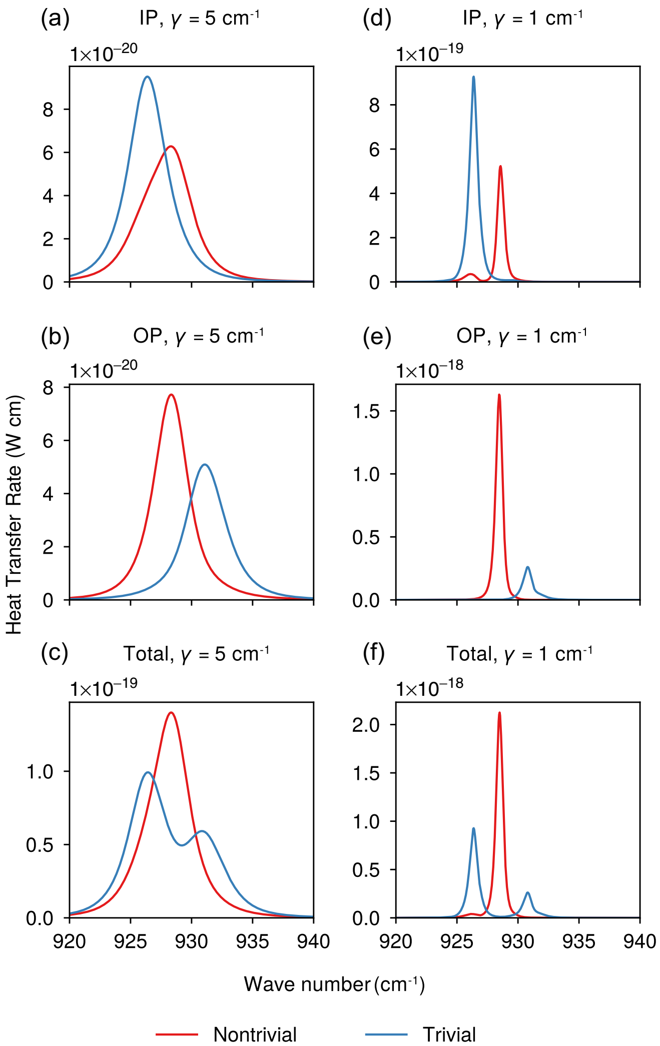

FIG. 9. The radiation heat transfer spectra between NP A and NP B in case II in (a) IP mode and (b) in OP mode, (c) the total power spectrum of the trivial and nontrivial lattice. [(d)–(f)] Net power spectra with decay rate $\gamma = 1\ \mathrm{cm}^{-1}$ in IP mode, OP mode and total.

topologically nontrivial lattice are $p_{\mathrm{net}}^{\mathrm{IP}}(\omega_{\mathrm{res}}) = 1.64 \times 10^{-19}$ W cm and $p_{\mathrm{net}}^{\mathrm{OP}}(\omega_{\mathrm{res}}) = 1.67 \times 10^{-19}\ \mathrm{W\,cm}^{-1}$ respectively, which are 1.42-fold enhancement in IP mode and 4.84-fold enhancement in OP mode. The frequencies where the peak p_{net} occur in both the IP mode and OP mode are close to the eigenfrequencies of the corner states in the nontrivial lattice [see in Fig. 9(a)] and the resonance frequency of the phonon polaritons of a single SiC NP. The power spectra of the topologically nontrivial lattice indicate that the excitation of the topological protected high-order TPhPs is responsible for radiative heat transfer between the NPs. For the trivial lattice, radiative heat transfer is dominated by bulk states in the lower-frequency band for IP mode and by bulk states in the higher-frequency band for OP mode, which is consistent with the numerical results obtained in the 1D SSH chain [41].

For the same purpose as in case I, here we artificially set the decay rate of the SiC NPs to be $\gamma = 1\ \mathrm{cm}^{-1}$. The real parts of the eigenfrequencies under $\gamma = 1\ \mathrm{cm}^{-1}$ are quite close to that of the original one, while the imaginary parts of the eigenfrequencies are mostly distributed near $-\gamma/2 = -0.5\ \mathrm{cm}^{-1}$ (not shown here). The radiative heat transfer spectra are shown in Fig. 9(b). The shapes of the power spectra are sharper due to the decrease in decay rate, and hence the contribution from different states is clearly seen. For the topologically nontrivial lattice, the corner states lying in the main gap dominate radiative heat transfer in OP mode in a topologically nontrivial lattice. For IP mode, two peaks appear in the power spectra, the one at $\omega = 928.5\ \mathrm{cm}^{-1}$ is the leading term originating from the topological corner states and the other at $\omega = 926.5\ \mathrm{cm}^{-1}$ is mainly contributed by those states right below the main gap. The spectral heat transfer rates between NP A and NP B at $\omega = \omega_{\mathrm{res}}$ in the nontrivial lattice are $5.04 \times 10^{-19}\ \mathrm{W\,cm}^{-1}$ in IP mode and $1.62 \times 10^{-18}\ \mathrm{W\,cm}^{-1}$ in OP mode, which are 51.24 folds and 1.88×10^{3} folds stronger than the trivial lattice under $\gamma = 1\ \mathrm{cm}^{-1}$. The severe contrast in spectral heat transfer rate at resonance frequency suggests the strong modulation of the heat transfer by high-order TPhPs in the nontrivial lattice.

By taking summation of the power spectra in IP mode and OP mode, the total net spectral radiative heat transfer is shown in Fig. 9(c), and the total radiative heat transfer power (integrated over the frequency range) is also calculated. The net radiative heat transfer powers is 6.45×10^{-17} W for the nontrivial lattice and 6.53×10^{-17} W for the trivial lattice, which is slightly larger than that of the nontrivial lattice. R_{mod} for IP and OP mode are 0.79 and 1.34 respectively and 0.98 in total under $\gamma = 5\ \mathrm{cm}^{-1}$. When setting the decay rate of SiC NP to $1\ \mathrm{cm}^{-1}$, the R_{mod} then becomes 0.47 in IP mode, 4.33 in OP mode and 1.39 in total. Generally, radiative heat transfer is suppressed in IP mode while enhanced in OP mode in the topologically nontrivial lattice. This is because, the emergence of TPhPs may suppress radiative heat transfer via the bulk states, the final effect of TPhPs on radiative heat transfer is the trade-off between the enhancing effects of extra TPhPs mode and the suppressing effects on bulk states. To be specific, the GF in OP mode involves a low-decay term ($1/r$ term), which allows high efficient radiative heat transfer between corner NPs, and hence the radiative heat transfer rate is enhanced in OP mode. While in IP mode, the GF decay in the power law of r^{-3} and the high-order TPhPs can only propagate in a relatively shorter range, resulting in a suppression in radiative heat transfer.

C. Case III

To better understand the effect of topological localized state as well as the topologically nontrivial boundaries in radiative heat transfer between NPs, we also investigate a nested lattice as illustrated in Fig. 3 (case III). In this case, the nontrivial 12×12 square region ($\beta = 0.75$), which is the same as in case I, is surrounded by a topologically trivial region ($\beta = 0.25$) that together form a larger square NP array (16×16). According to the bulk-boundary correspondence, the topologically protected edge states will also appear in the four sides in the inner square. At the same time, in the nontrivial lattice, the high-order corner states are also expected to emerge. Similarly, we also numerically calculate the properties of the corresponding trivial lattice.

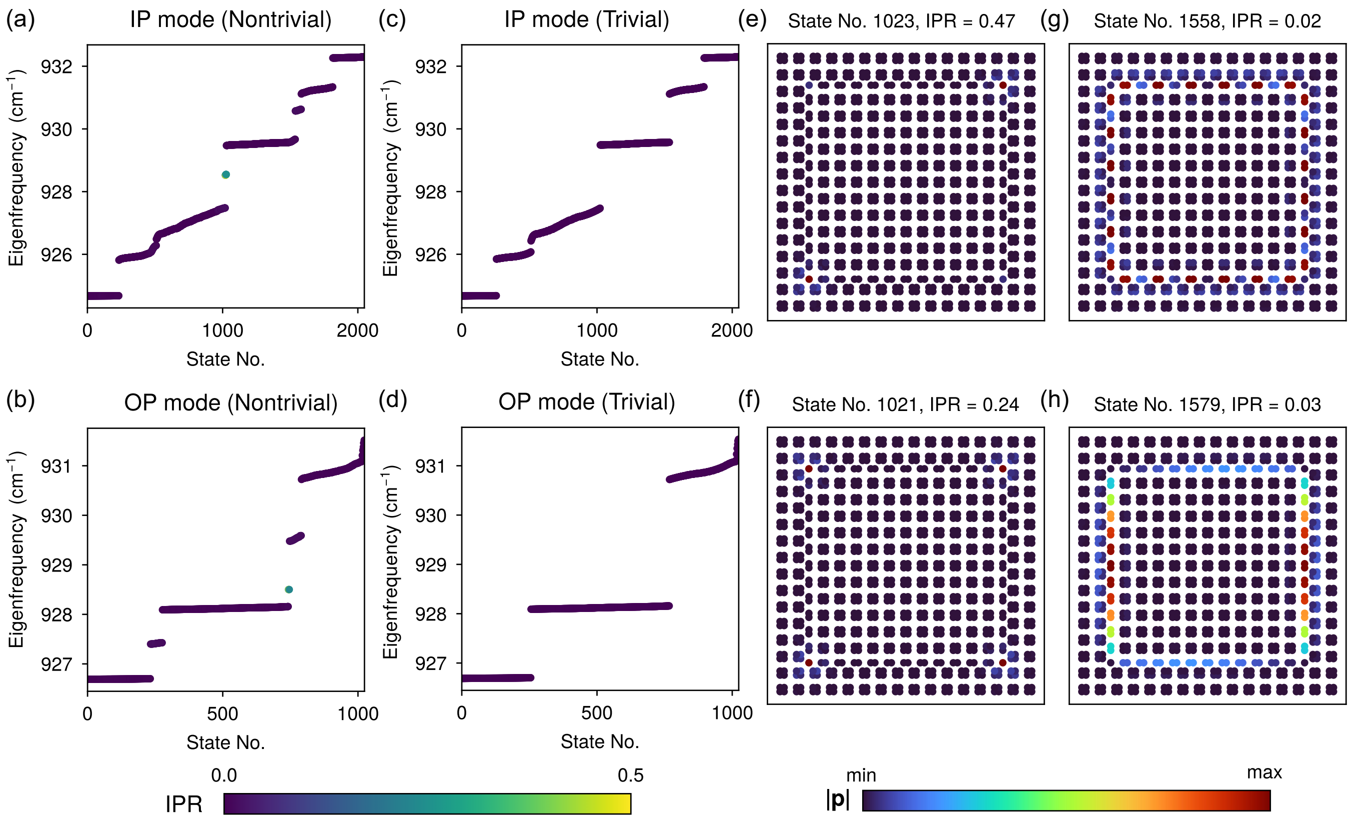

FIG. 10. Band structures and dipole moment distributions of the nested square lattices (case III). (a) the IP mode and (b) the OP mode band structures of the lattice with topologically nontrivial configuration, (c) the IP mode, and (d) the OP mode band structures of the lattice with topologically trivial configuration. [(e) and (f)] Dipole moment distributions of corner states in IP mode, (g) and (h) the dipole moment distributions of the edge states in IP mode.

The band structures of the topologically nontrivial lattice are shown in Figs. 10(a) and 10(b), and the band structures of the topologically trivial lattice are shown in Figs. 10(c) and 10(d), the colors are mapped from the IPRs of the corresponding states. Similar to the previous cases, the states with higher IPRs can be observed in the gap of the band structures in OP mode and IP mode of the topologically nontrivial lattice, bulk bands in the band structure are almost consistent with that of the topologically trivial lattice. In the main gap near the resonance frequency, there are eight almost degeneracy corner states in IP mode and four in OP mode. We take the corner states in IP mode as an example for analysis, the state No. of these states are 1020–1027 with IPRs being 0.24, 0.24, 0.47, 0.47, 0.23, 0.23, 0.25, and 0.25 respectively. These states can be categorized into two groups, one with IPR $\sim 1/4$ (No. 1020, 1021, and 1024–1027) implying the dipole moment distributions are localized over 4 NPs and the other group of states has IPR $\sim 1/2$ (No. 1022 and 1023) implying the dipole moment distributions are localized over 2 NPs. The dipole moment distributions of the two kinds of states are plotted in Figs. 10(e) and 10(f), in Fig. 10(e) the dipole moment distribution is localized over the diagonal NPs in the topologically nontrivial region and decay rapidly in space, and in Fig. 10(f) the dipole moment distribution is localized over the four corner NPs in the inner region. These states, beyond the bulk-boundary correspondence, are topologically protected high-order localized states. In Figs. 10(g) and 10(h), we also plot two kinds of edge states, in one of which [Fig. 10(g)], the dipole moment distribution is localized over two sides of the square-shaped interface between the topologically nontrivial and trivial region, and in the other kind the dipole moment distribution is localized over all the four sides.

The radiative transfer rates from NP A to NP C are shown in Figs. 11(a)–11(c). R_{mod} in this case are 0.92 in IP mode, 1.12 in OP mode, and 1.01 in total, the modulation ratios become 0.60, 1.91, and 1.27 respectively after setting the decay rate to 1 cm^{-1}. We can observe in Fig. 11(a) that there are two peaks in the radiative power spectrum of the nontrivial lattice (the red solid line in the figure), the corresponding frequencies are 926.13 and 928.61 cm^{-1}, respectively. Contribution from the low-frequency bulk states is comparable and even stronger than from the TPhPs, which essentially correspond to the eigenstates lying at the edges of the lower bands with high group velocity. In OP mode, radiative heat transfer is also dominated by the corner states in main gap, but the enhancement is weaker than in case II, owing to the split of dipole moment in four NPs rather than two NPs in one of the corner states. From the calculation, we can also find that the edge states seem to have little effect on radiative heat transfer between NP A and NP B. This phenomenon is reasonable from the point of the dipole moment distributions of these edge states, Figs. 11(f) and 11(g) suggest that for both of the two kinds of edge states, the dipole moment distributions are localized mostly over the center of the edges and decay

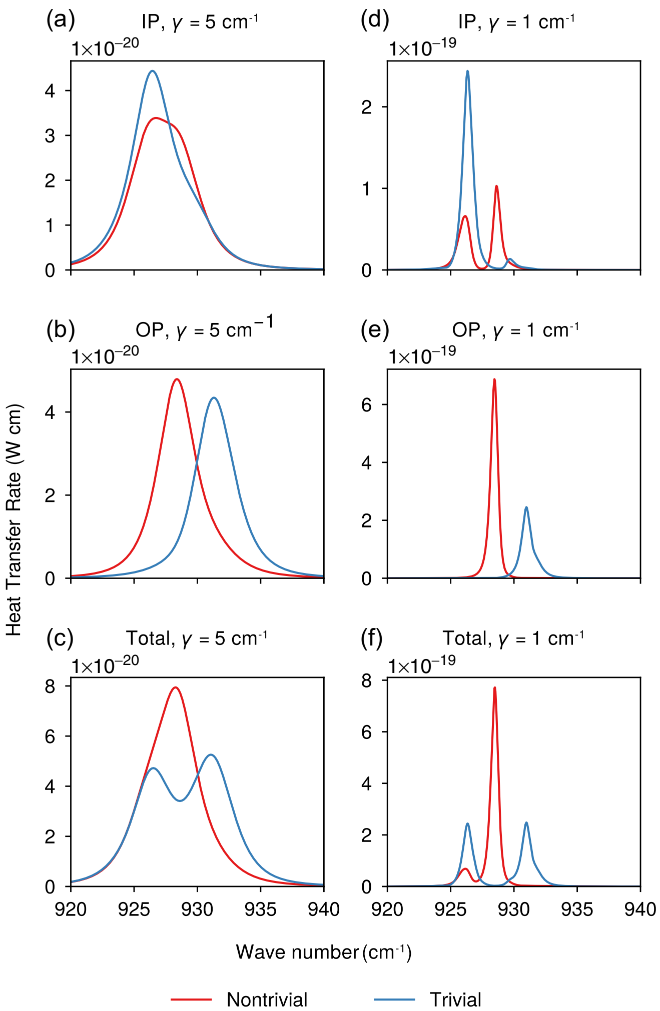

FIG. 11. The radiation heat transfer spectra between NP A and NP C in case III in (a) IP mode and (b) in OP mode, (c) the total power spectrum of the trivial and nontrivial lattice. [(d)–(f)] Net power spectra with decay rate $\gamma = 1$ cm^{-1} in IP mode, OP mode, and total.

smoothly along the interface of the topologically nontrivial and trivial region. In this manner, the dipole moments at the corner NPs of edge states is not that strong as in corner states and hence the radiative heat transfer contribution is negligible.

IV. ROBUSTNESS

In this section, we study the robustness of high-order TPhPs and its role in radiative heat transfer. Again, we set the decay rate of the SiC NPs to 1 cm^{-1} to exclude the effects of the bulk states. Firstly, we create a defect in the lattice by removing two NPs in the center of the connecting interface as illustrated in Fig. 12(a) and labeled as No. 1. Four corner states are maintained in the OP band structure of the nontrivial lattice, and the power spectrum is almost the same as the nondefected one. It is worth mentioning that there are extra two highly localized states with IPRs also close to 1/2 in the gap, however the dipole moment distributions of the two states are localized over the adjacent NPs on the left and right side of the missing NPs and hence have little contribution to radiative heat transfer between the corner NPs. When the same defect is introduced to the lattice with topologically trivial configuration, the defect states also emerge in the band gap and make negligible difference on the power spectrum.

We then create a stronger defect on the lattices by removing the NP next to the corner NP (No. 2 in Fig. 12), which breaks the mirror symmetry and partially the sublattice symmetry on the lattices. In this manner, only three of the corner states are preserved with two extra defect states generated in the band gap. IPR of one of the corner states is 0.84, exceeding 1/2, indicating that the dipole moment distribution is localized mostly over one of the corner NPs (NP A). As aforementioned, the dipole moment distributions of the defect states are mainly localized over the NPs near the lattice site of the missing NP, this makes radiative heat transfer between the corner NPs even slightly enhanced compared to the nondefected lattice. It is worth mentioning that the defect states in the topologically trivial lattice also affects the net power and also a frequency shift on the power spectrum, which is not observed in the nontrivial lattice.

By randomly changing the positions of the NPs in the lattice within the xy plane, disorder is then introduced to the joint 2D SSH lattice. We consider the maximum relative displacement to the average distance between the NPs ($a_x/2$) as an indicator of the degree of disorder, and keep the maximum relative displacement lower than 3% to ensure the validity of the coupled dipole model. Crucially, the mirror symmetry and sublattice symmetry are broken once the disorder is introduced, such that the IPRs of the states may be larger than 1/2 and the degeneracies of the corner states are lifted [76]. Figures 12(d) and 12(e) plot a set of eigenfrequencies spectra under different maximum disorders in OP and IP mode, every single column in the figure has a corresponding lattice structure. Notice that the eigenfrequencies spectra in each column is chosen from 100 realizations (not shown here) for the same level of disorder as an instance. We can see in the figures that the corner states lying near the resonance frequency remains well isolated on the midgap despite the edge states merging with the bulk states as the degree of disorder increasing, and the eigenfrequencies of these corner states are always near ω_{res}. The robustness of the topologically nontrivial lattice can also be confirmed in view of the total radiative heat transfer rate p_{net}. By carrying out multiple calculations of p_{net} in the topologically trivial and nontrivial lattices with the maximum relative displacement being 1%, 2%, and 3% respectively and averaging the results, the average spectral radiative heat transfer rates are obtained, which show little difference between the radiative heat transfer spectra of the topologically trivial and nontrivial lattice. The radiative heat transfer spectra under different degree of disorder are identical with that of the corresponding ordered lattices. To better obtain the robustness regarding the radiative heat transfer rate, in this manuscript we consider the calculation of the radiative heat transfer rate as an independent repeated trail with p_{net} being the independent variable, and study the statistical characteristics regarding p_{net} between the NPs in the topologically trivial and not rival lattices. For topologically nontrivial lattices, the distributions of p_{net} obtained in each numerical calculation tend to be less fluctuated than the topologically trivial ones under the same

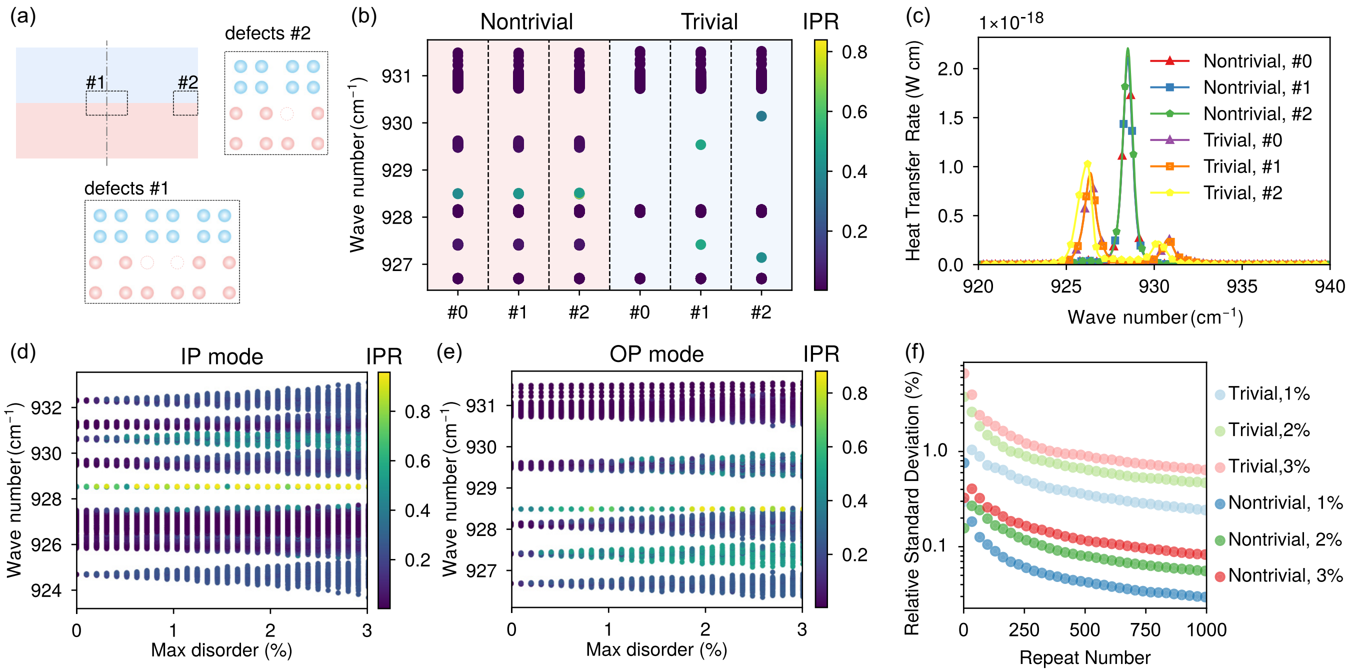

FIG. 12. (a) Schematic of defects by removing NPs in the lattice site, (b) OP mode band structure and (c) total radiative heat transfer rate under different defects. (d) IP mode and (e) OP mode band structures with max relative disorder ranges from 0% to 3%, (f) RSDs of the net radiative heat transfer rate in disordered topologically trivial and nontrivial lattice in case II, the maximum relative displacements are 1%, 2%, and 3%.

degree of disorder (not shown here). To numerically study the difference in the degree of fluctuation between the $p_{\rm net}$ of the topologically trivial and nontrivial lattices, we calculated the relative standard deviations (RSDs) as the number of repeated calculation increasing. The results are obtained after carrying out 1000 realizations of independent repeated trials and are illustrated in Fig. 12(f), in which the data points in light colors are the results from topologically trivial lattice and in dark colors are the results from topologically nontrivial lattice. The results indicate that for the topologically nontrivial lattice, the RSDs are much lower under the same degree of disorder. To be specific, RSDs of the net radiative heat transfer power between NPs in topologically nontrivial lattice are $\sim$1/8 of that in the topologically trivial lattice.

V. CONCLUSIONS

In summary, we study the topological properties as well as radiative heat transfer behavior in 2D NP arrays which mimics the 2D SSH model. The band structures, which take into account the near- and far-field dipole-dipole interactions, of the 2D SSH lattices under PBC are calculated. We use 2D Zak phases to characterize the topological properties of the lattices under PBCs and obtained the topological phases as a function of β. By applying OBCs to the topologically nontrivial lattices, we confirm the existence of TPhPs and high-order TPhPs protected by the nonzero 2D Zak phases, which are consistent with the bulk-edge-corner correspondence. The roles of TPhPs paly in NFRHT between NPs are revealed by constructing three cases of finite lattices with different interfaces between topologically trivial and nontrivial regions, in which the power spectra are analyzed in IP and OP modes separately. The results indicate that high-order TPhPs show considerable capability in modulating NFRHT between certain NPs in the 2D SSH lattices. We also find that the emergence of high-order TPhPs as well as the modulation effects show a moderate robustness by introducing perturbation into the lattices.

ACKNOWLEDGMENTS

This work is supported by the National Natural Science Foundation of China (Grants No. 52120105009, No. 52276078, and No. 52090063), Science and Technology Commission of Shanghai Municipality (Grants No. 20JC1414800 and No. 22ZR1432900) and the Fundamental Research Funds for the Central Universities. We also thank the support from Shanghai Jiao Tong University 2030 Initiative.

APPENDIX A: THE CALCULATION OF 2D ZAK PHASE

The 2D Zak phase can be used to characterize the topological feature of the infinite 2D SSH lattice, which can be calculated as

$$\theta_j = -\frac{1}{2}\int_{\rm FBZ} d^2\mathbf{k}\ {\rm Tr}[A_j(\mathbf{k})],\ \ j = x, y, \tag{A1}$$

where $(A_j)_{mn}(\mathbf{k}) = {\rm i}\langle \mathbf{u}^L_{m\mathbf{k}}|\partial k_j|\mathbf{u}_{n\mathbf{k}}\rangle$ with $|\mathbf{u}_{n\mathbf{k}}\rangle$ denoting the periodic part of the Bloch function of the nth band. We apply Wilson loop approach to numerically calculate it, the discrete solution to the cumulative Berry phase can be expressed as

$$\theta_i = \frac{a_i}{2\pi}\int dk_j\ v_i^n(k_j),\ \{i, j\}_{i\neq j} \in \{x, y\}, \tag{A2}$$

where v_i^n is the nth eigenvalue of the Wannier Hamiltonian

$$H_{w,i}(\mathbf{k}) = -{\rm i}\log \Pi_{q=0}^{M}\big[F_{i,\mathbf{k}+q\Delta k_i}\big] \tag{A3}$$

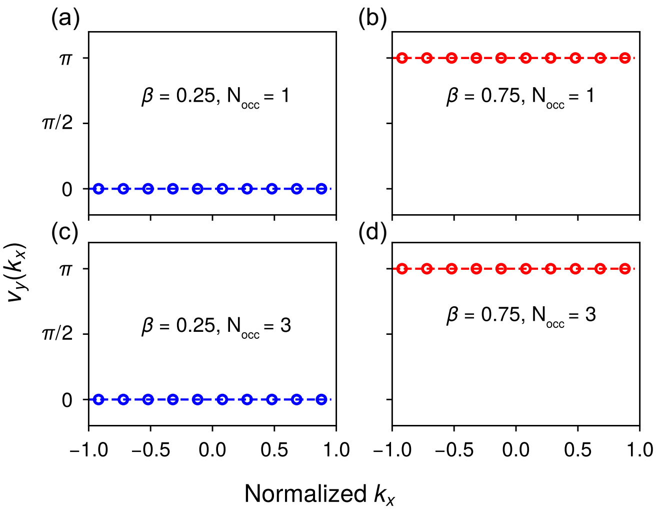

FIG. 13. Wannier bands $v_y(k_x)$ of the first band gap for the case under (a) $\beta = 0.25$ and (b) $\beta = 0.75$, as well as the third band gap for (c) $\beta = 0.25$ and (d) $\beta = 0.75$.

in which M satisfying $(M+1)\Delta k_i = 2\pi/d$, and

$$\left[F_{i,\mathbf{k}+q\Delta k_i}\right]_{mn} = \left\langle \mathbf{u}^L_{m,\mathbf{k}} \middle| \mathbf{u}_{n,\mathbf{k}^R+\Delta k_j} \right\rangle \tag{A4}$$

for $m, n \in \{1, 2, 3, \ldots, N_{\text{occ}}\}$, where N_{occ} is the number of the bands below the band gap.

Here we take the OP mode band structure as a demonstration. The Wannier bands, i.e., v_i as a function of k_j, are shown in Fig. 13. The numerical result indicates that the lattice with $\beta = 0.75$ has topologically nontrivial phases ($\theta_y = \pi$) in first and third band, while the lattice with $\beta = 0.25$ is topologically trivial ($\theta_y = 0$). θ_x for the 2 infinite lattices is exactly the same as θ_x owing to the C_4 symmetry. According to Eq. (A2), the 2D Zak phase is then obtained, for the topologically trivial lattice $\theta_x = \theta_y = 0$ and for the nontrivial lattice $\theta_x = \theta_y = \pi$.

APPENDIX B: THE CALCULATION OF SLOW CONVERGENCE TERMS IN GF

Here we take the OP component of the $\mathbf{G_k}$ as an example, in which the diagonal terms can be expressed as

$$\begin{aligned}\hat{G}^{\text{OP}}_{\mathbf{k},ii} &= \sum_{\substack{m,n\in\mathbb{Z},\\ \mathbf{R}_{mn}\neq 0}} \frac{e^{ik_0R_{mn}+i\mathbf{k}\cdot\mathbf{R}_{mn}}}{4\pi}\left[-ik_0\sum_{l=1}^{3}\left(\frac{i}{k_0R_{mn}}\right)^l\right]\\ &= \sum_{l=1}^{3}\sum_{\substack{m,n\in\mathbb{Z},\\ \mathbf{R}_{mn}\neq 0}} \frac{k_0 e^{ik_0R_{mn}+i\mathbf{k}\cdot\mathbf{R}_{mn}}}{4\pi i}\left(\frac{i}{k_0R_{mn}}\right)^l\end{aligned} \tag{B1}$$

and the off-diagonal terms can be written as

$$\begin{aligned}\hat{G}^{\text{OP}}_{\mathbf{k},ij} &= \sum_{m,n\in\mathbb{Z}} \frac{e^{ik_0S_{mn}+i\mathbf{k}\cdot\mathbf{R}_{mn}}}{4\pi}\left[-ik_0\sum_{l=1}^{3}\left(\frac{i}{k_0S_{mn}}\right)^l\right]\\ &= \sum_{l=1}^{3}\sum_{m,n\in\mathbb{Z}} \frac{k_0 e^{ik_0S_{mn}+i\mathbf{k}\cdot\mathbf{R}_{mn}}}{4\pi i}\left(\frac{i}{k_0S_{mn}}\right)^l\end{aligned} \tag{B2}$$

For both the diagonal and off-diagonal terms, the series can be regarded as the summation of three subseries, i.e., for $l = 1, 2, 3$. For the subseries of $l = 2$ and 3, the terms in the subseries decay with $1/R^2$ and $1/R^3$, resulting in a fast convergence in real space. Thus, these two subseries are calculated in real space. We now consider the subseries of $l = 1$. Let

$$Q(\mathbf{r},\mathbf{k}) = \sum_{m,n\in\mathbb{Z}} \frac{e^{ik_0|\mathbf{r}-\mathbf{R}_{mn}|}}{4\pi|\mathbf{r}-\mathbf{R}_{mn}|}e^{i\mathbf{k}\cdot\mathbf{R}_{mn}}, \tag{B3}$$

where $\mathbf{r}$ is a 3D vector in real space and $r = |\mathbf{r}|$, the diagonal and off-diagonal terms can be further written as,

$$\hat{G}^{\text{OP},l=1}_{ii} = \lim_{r\to 0} Q(\mathbf{r},\mathbf{k}) - \lim_{r\to 0}\frac{e^{ik_0r}}{4\pi r}, \tag{B4}$$

$$\hat{G}^{\text{OP},l=1}_{ij} = Q(\mathbf{s}_{ij},\mathbf{k}). \tag{B5}$$

1. The calculation of slowly convergent series in the diagonal terms

According to the Poisson's summation formula, the summation in Eq. (B3) can be written in the form of summation in reciprocal space, i.e.,

$$Q(\mathbf{r},\mathbf{k}) = \frac{1}{\Omega}\sum_{m,n\in\mathbb{Z}} F(\mathbf{k}+\mathbf{q}_{mn})e^{i(\mathbf{q}_{mn}+\mathbf{k})\cdot\mathbf{r}}, \tag{B6}$$

where $\mathbf{q}_{mn}$ is the reciprocal lattice vector, $\Omega = a_xa_y$ is the area of the unit cell in real space, and $F(\mathbf{k}+\mathbf{q}_{mn})$ is the 2D Fourier transform of the function $e^{ik_0|\mathbf{r}-\mathbf{R}_{mn}|}/|\mathbf{r}-\mathbf{R}_{mn}|$, which gives

$$F(\mathbf{k}+\mathbf{q}_{mn}) = \iint d\mathbf{r}\, e^{-(\mathbf{k}+\mathbf{q}_{mn})\cdot\mathbf{r}}\frac{e^{ik_0|\mathbf{r}-\mathbf{R}_{mn}|}}{|\mathbf{r}-\mathbf{R}_{mn}|} = \frac{2\pi i e^{ik_zz}}{k_z}, \tag{B7}$$

where z is the z component of r and $k_z = \sqrt{k_0^2 - |\mathbf{k}+\mathbf{q}_{mn}|^2}$, $\text{Im}(k_z) > 0$. Putting Eqs. (B7) and (B6) into Eq. (B4), we have

$$\hat{G}^{\text{OP},l=1}_{ii} = \frac{1}{4\pi}\lim_{z\to 0^+}\left(\frac{2\pi i}{\Omega}\sum_{m,n\in\mathbb{Z}}\frac{e^{ik_zz}}{k_z} - \frac{e^{ik_0z}}{z}\right). \tag{B8}$$

When $\mathbf{k} = \mathbf{0}$, the real part of $\hat{G}^{\text{OP},l=1}_{ii}$ is a finite value under the limit of $k_0 \to 0$ and $z \to 0^+$, which gives [77]

$$\begin{aligned}D &= \text{Re}\left(\hat{G}^{\text{OP},l=1}_{ii}\right)_{\mathbf{k}=0}\\ &= \lim_{z\to 0^+}\frac{1}{4\pi}\left(\frac{2\pi}{\Omega}\sum_{m,n\in\mathbb{Z}}\frac{e^{-z|\mathbf{q}_{mn}|}}{|\mathbf{q}_{mn}|} - \frac{1}{z}\right),\end{aligned} \tag{B9}$$

where $D = -3.9002/(4\pi d)$ for square lattice (in this paper $d = a_x = a_y$), representing a geometrical effect which is independent of $\mathbf{r}$ and $\mathbf{k}$ [78].

Subtracting the RHS of Eq. (B9) and adding the value of D in Eq. (B8), we have

$$\begin{aligned}\hat{G}^{\text{OP},l=1}_{ii} &= \frac{1}{2\Omega}\sum_{\substack{m,n\in\mathbb{Z},\\ \mathbf{R}_{mn}\neq 0}}\left(\frac{1}{\sqrt{|\mathbf{q}_{mn}+\mathbf{k}|^2-k_0^2}} - \frac{1}{|\mathbf{q}_{mn}|}\right)\\ &\quad + D + \frac{i}{2\Omega\sqrt{k_0^2-|k|^2}} - \frac{ik_0}{4\pi}.\end{aligned} \tag{B10}$$

The subseries now realize a quick convergence within a small circle with radius a few hundred reciprocal-lattice constant.

2. The calculation of slowly convergent series in the off-diagonal terms

Since all the NPs are aligned in xy plane, the z component of $\mathbf{s}_{ij}$ is also 0. We now consider Eq. (B3) in 2D space in the form of Hankel function:

$$Q(\mathbf{r},\mathbf{k}) = \sum_{m,n\in\mathbb{Z}} \frac{\mathrm{i}k_0 h_0(k_0|\mathbf{r}-\mathbf{R}_{mn}|)}{4\pi} \mathrm{e}^{\mathrm{i}\mathbf{k}\cdot\mathbf{R}_{mn}}, \tag{B11}$$

in which $\mathbf{R}_{mn}$ is the 2D lattice vector in real space, $\mathbf{r}=\mathbf{s}_{ij}$ is a nonzero 2D vector coplanar with $\mathbf{R}_{mn}$, and $h_0[\cdot]$ is the spherical Hankel function of order 0. By making use of the integral identity for $h_0(k_0|\mathbf{r}-\mathbf{R}_{mn}|)$ and the introducing of splitting parameter of E, $Q(\mathbf{r},\mathbf{k})$ can be split into two parts, i.e.,

$$\begin{aligned} Q(\mathbf{r},\mathbf{k}) =& \frac{1}{4\pi}\sum_{m,n\in\mathbb{Z}} \mathrm{e}^{\mathrm{i}\mathbf{k}\cdot\mathbf{R}_{mn}} \frac{2}{\sqrt{\pi}} \int_0^\infty ds \exp\left[-|\mathbf{r}-\mathbf{R}_{mn}|^2 s^2 + \frac{k_0^2}{4s^2}\right] \\ =& \frac{1}{4\pi}\sum_{m,n\in\mathbb{Z}} \mathrm{e}^{\mathrm{i}\mathbf{k}\cdot\mathbf{R}_{mn}} \frac{2}{\sqrt{\pi}} \int_0^E ds \exp\left[-|\mathbf{r}-\mathbf{R}_{mn}|^2 s^2 + \frac{k_0^2}{4s^2}\right] (\text{denoted as } Q_1(\mathbf{r},\mathbf{k})) \\ &+ \frac{1}{4\pi}\sum_{m,n\in\mathbb{Z}} \mathrm{e}^{\mathrm{i}\mathbf{k}\cdot\mathbf{R}_{mn}} \frac{2}{\sqrt{\pi}} \int_E^\infty ds \exp\left[-|\mathbf{r}-\mathbf{R}_{mn}|^2 s^2 + \frac{k_0^2}{4s^2}\right] (\text{denoted as } Q_2(\mathbf{r},\mathbf{k})), \end{aligned} \tag{B12}$$

in which the first term converges fast in reciprocal space while the second terms converges fast in reciprocal space.

The integral in $Q_2(\mathbf{r},\mathbf{k})$ can be further simplified and calculated in the form of complementary error functions (erfc):

$$Q_2(\mathbf{r},\mathbf{k}) = \frac{1}{8\pi}\sum_{m,n\in\mathbb{Z}} \frac{\mathrm{e}^{\mathrm{i}\mathbf{k}\cdot\mathbf{R}_{mn}}}{|\mathbf{r}-\mathbf{R}_{mn}|}\left[\mathrm{e}^{\mathrm{i}k_0|\mathbf{r}-\mathbf{R}_{mn}|}\mathrm{erfc}\left(|\mathbf{r}-\mathbf{R}_{mn}|E + \frac{\mathrm{i}k_0}{2E}\right) + \text{c.c.}\right], \tag{B13}$$

where c.c. stands for the complex conjugate.

$Q_1(\mathbf{r},\mathbf{k})$ can be calculated in reciprocal space by applying the Poisson's summation formula [35,77]. To be exact,

$$\begin{aligned} Q_1(\mathbf{r},\mathbf{k}) =& \frac{1}{4\pi}\sum_{m,n\in\mathbb{Z}} \mathrm{e}^{\mathrm{i}\mathbf{k}\cdot\mathbf{R}_{mn}} \frac{2}{\sqrt{\pi}} \int_0^E ds \exp\left[-|\mathbf{r}-\mathbf{R}_{mn}|^2 s^2 + \frac{k_0^2}{4s^2}\right] \\ =& \frac{1}{4\pi}\frac{2}{\sqrt{\pi}}\int_0^E ds\, \mathrm{e}^{k_0^2/4s^2+\mathrm{i}\mathbf{k}\cdot\mathbf{r}} \sum_{m,n\in\mathbb{Z}} \frac{1}{\Omega} F(\mathbf{k}+\mathbf{q}_{mn})\mathrm{e}^{\mathrm{i}\mathbf{q}_{mn}\cdot\mathbf{r}}, \end{aligned} \tag{B14}$$

in which $F(\mathbf{k}+\mathbf{q}_{mn})$ denotes the 2D Fourier transform of $\mathrm{e}^{-|\mathbf{r}-\mathbf{R}_{mn}|^2 s^2}$, which can be calculated as

$$F(\mathbf{k}+\mathbf{q}_{mn}) = \iint d\mathbf{r}\, \mathrm{e}^{-\mathrm{i}\mathbf{k}\cdot\mathbf{r}} \mathrm{e}^{-|\mathbf{r}-\mathbf{R}_{mn}|^2 s^2} = \frac{\pi}{s^2}\exp\left(-\frac{|\mathbf{k}+\mathbf{q}_{mn}|^2}{4s^2}\right). \tag{B15}$$

Thus we have

$$\begin{aligned} Q_1(\mathbf{r},\mathbf{k}) =& \frac{2}{\Omega\sqrt{\pi}}\sum_{m,n\in\mathbb{Z}} \mathrm{e}^{\mathrm{i}(\mathbf{k}+\mathbf{q}_{mn})\cdot\mathbf{r}} \int_0^E \frac{ds}{s^2}\exp\left(\frac{k_0^2-|\mathbf{k}+\mathbf{q}_{mn}|^2}{4s^2}\right) \\ =& \frac{2}{\Omega\sqrt{\pi}}\sum_{m,n\in\mathbb{Z}} \mathrm{e}^{\mathrm{i}(\mathbf{k}+\mathbf{q}_{mn})\cdot\mathbf{r}} \int_{1/E}^\infty ds \exp\left(\frac{k_0^2-|\mathbf{k}+\mathbf{q}_{mn}|^2}{4}s^2\right) (\text{let } s\to 1/s). \end{aligned} \tag{B16}$$

Equation (B16) is now similar to $Q_2(\mathbf{r},\mathbf{k})$ in Eq. (B12) and can be manipulated similarly to be in the form of complementary error function,

$$Q_1(\mathbf{r},\mathbf{k}) = \frac{\mathrm{i}}{4\Omega}\sum_{m,n\in\mathbb{Z}} \frac{\mathrm{e}^{\mathrm{i}(\mathbf{k}+\mathbf{q}_{mn})\cdot\mathbf{r}}}{\sqrt{k_0^2-|\mathbf{k}+\mathbf{q}_{mn}|^2}}\left[\mathrm{erfc}\left(\frac{-\mathrm{i}\sqrt{k_0^2-|\mathbf{k}+\mathbf{q}_{mn}|^2}}{2E}\right) + \text{c.c.}\right]. \tag{B17}$$

The splitting parameter E is optimally chosen such that Q_1 and Q_2 do not differ by more than several orders of magnitude. In this paper, we choose $E = \sqrt{\frac{\pi}{\Omega}}$ according to Ref. [77].

[1] S. M. Bhattacharjee, M. Mj, and A. Bandyopadhyay, *Topology and Condensed Matter Physics* (Springer, Singapore, 2017), Vol. 19.

[2] M. Z. Hasan and C. L. Kane, Colloquium: Topological insulators, Rev. Mod. Phys. **82**, 3045 (2010).

[3] X. Gu, Y. Wei, X. Yin, B. Li, and R. Yang, Colloquium: Phononic thermal properties of two-dimensional materials, Rev. Mod. Phys. **90**, 041002 (2018).

[4] V. Lahtinen and J. Pachos, A short introduction to topological quantum computation, SciPost Phys. **3**, 021 (2017).

[5] A. Stern and N. H. Lindner, Topological quantum computation—from basic concepts to first experiments, Science **339**, 1179 (2013).

[6] S. Das Sarma, M. Freedman, and C. Nayak, Topological quantum computation, Phys. Today **59**(7), 32 (2006).

[7] J. Yao, J. Shao, Y. Wang, Z. Zhao, and G. Yang, Ultra-broadband and high response of the Bi_2Te_3–Si heterojunction and its application as a photodetector at room temperature in harsh working environments, Nanoscale **7**, 12535 (2015).

[8] J. Yao, Z. Zheng, and G. Yang, Layered-material WS2/ Topological Insulator Bi_2Te_3 Heterostructure Photodetector with Ultrahigh Responsivity in the Range from 370 to 1550 Nm, J. Mater. Chem. C **4**, 7831 (2016).

[9] X. Zhang, J. Wang, and S.-C. Zhang, Topological insulators for high-performance terahertz to infrared applications, Phys. Rev. B **82**, 245107 (2010).

[10] J. Son, K. Banerjee, M. Brahlek, N. Koirala, S.-K. Lee, J.-H. Ahn, S. Oh, and H. Yang, Conductance modulation in topological insulator Bi_2Se_3 thin films with ionic liquid gating, Appl. Phys. Lett. **103**, 213114 (2013).

[11] H. C. P. Movva, A. Rai, S. Kang, K. Kim, B. Fallahazad, T. Taniguchi, K. Watanabe, E. Tutuc, and S. K. Banerjee, High-mobility holes in dual-gated WSe_2 field-effect transistors, ACS Nano **9**, 10402 (2015).

[12] H. Zhu, E. Zhao, C. A. Richter, and Q. Li, Topological Insulator Bi_2Se_3 nanowire field effect transistors, ECS Transactions **64**, 51 (2014).

[13] B. I. Halperin, Quantized hall conductance, current-carrying edge states, and the existence of extended states in a two-dimensional disordered potential, Phys. Rev. B **25**, 2185 (1982).

[14] M. Kim, Z. Jacob, and J. Rho, Recent Advances in 2D, 3D and higher-order topological photonics, Light Sci. Appl. **9**, 130 (2020).

[15] M. Jung, Y. Yu, and G. Shvets, Exact higher-order bulk-boundary correspondence of corner-localized states, Phys. Rev. B **104**, 195437 (2021).

[16] L. Trifunovic, Bulk-and-edge to corner correspondence, Phys. Rev. Res. **2**, 043012 (2020).

[17] B.-Y. Xie, G.-X. Su, H.-F. Wang, H. Su, X.-P. Shen, P. Zhan, M.-H. Lu, Z.-L. Wang, and Y.-F. Chen, Visualization of higher-order topological insulating phases in two-dimensional dielectric photonic crystals, Phys. Rev. Lett. **122**, 233903 (2019).

[18] C. He, X. Ni, H. Ge, X.-C. Sun, Y.-B. Chen, M.-H. Lu, X.-P. Liu, and Y.-F. Chen, Acoustic topological insulator and robust one-way sound transport, Nat. Phys. **12**, 1124 (2016).

[19] H. Xue, Y. Yang, F. Gao, Y. Chong, and B. Zhang, Acoustic higher-order topological insulator on a kagome lattice, Nat. Mater. **18**, 108 (2019).

[20] H. Fan, B. Xia, L. Tong, S. Zheng, and D. Yu, Elastic higher-order topological insulator with topologically protected corner states, Phys. Rev. Lett. **122**, 204301 (2019).

[21] H. Fan, B. Xia, S. Zheng, and L. Tong, Elastic phononic topological plate with edge and corner sates based on pseudospin-valley-coupling, J. Phys. D **53**, 395304 (2020).

[22] X.-D. Chen, W.-M. Deng, F.-L. Shi, F.-L. Zhao, M. Chen, and J.-W. Dong, Direct observation of corner states in second-order topological photonic crystal slabs, Phys. Rev. Lett. **122**, 233902 (2019).

[23] S. Mittal, V. V. Orre, G. Zhu, M. A. Gorlach, A. Poddubny, and M. Hafezi, Photonic Quadrupole Topological Phases, Nat. Photonics **13**, 692 (2019).

[24] Y. Chen, F. Meng, Z. Lan, B. Jia, and X. Huang, Dual-Polarization second-order photonic topological insulators, Phys. Rev. Appl. **15**, 034053 (2021).

[25] Y. Chen, Z. Lan, J. Li, and J. Zhu, Topologically protected second harmonic generation via doubly resonant high-order photonic modes, Phys. Rev. B **104**, 155421 (2021).

[26] M.-C. Jin, Y.-F. Gao, H.-Z. Lin, Y.-H. He, and M.-Y. Chen, Corner states in second-order two-dimensional topological photonic crystals with reversed materials, Phys. Rev. A **106**, 013510 (2022).

[27] Y. Chen, Z.-K. Lin, H. Chen, and J.-H. Jiang, Plasmon-polaritonic quadrupole topological insulators, Phys. Rev. B **101**, 041109(R) (2020).

[28] Y. Ota, F. Liu, R. Katsumi, K. Watanabe, K. Wakabayashi, Y. Arakawa, and S. Iwamoto, Photonic crystal nanocavity based on a topological corner state, Optica **6**, 786 (2019).

[29] M. Kim and J. Rho, Topological edge and corner states in a two-dimensional photonic Su-Schrieffer-Heeger lattice, Nanophotonics **9**, 3227 (2020).

[30] Z. Wang, Y. Chong, J. D. Joannopoulos, and M. Soljačić, Observation of unidirectional backscattering-immune topological electromagnetic states, Nature (London) **461**, 772 (2009).

[31] F. Yi, M. Q. Liu, N. N. Wang, B. X. Wang, and C. Y. Zhao, Near-field observation of mid-infrared edge modes in topological photonic crystals, Appl. Phys. Lett. **123**, 081110 (2023).

[32] X. Zhang, Y. Zhou, X. Sun, X. Zhang, M.-H. Lu, and Y.-F. Chen, Reconfigurable light imaging in photonic Higher-Order Topological Insulators, Nanomaterials **12**, 819 (2022).

[33] M. Chao, Q. Liu, W. Zhang, L. Zhuang, and G. Song, Mutual coupling of corner-localized quasi-BICs in high-order topological PhCs and sensing applications, Opt. Express **30**, 29258 (2022).

[34] J. Wu, S. Ghosh, Y. Gan, Y. Shi, S. Mandal, H. Sun, B. Zhang, T. C. H. Liew, R. Su, and Q. Xiong, Higher-order topological Polariton corner state Lasing, Sci. Adv. **9**, eadg4322 (2023).

[35] B. X. Wang and C. Y. Zhao, High-order topological quantum optics in ultracold atomic metasurfaces, arXiv:2108.01509.
[36] P. Ben-Abdallah, S.-A. Biehs, and K. Joulain, Many-body radiative heat transfer theory, Phys. Rev. Lett. **107**, 114301 (2011).
[37] J. Dong, J. Zhao, and L. Liu, Radiative heat transfer in many-body systems: coupled electric and magnetic dipole approach, Phys. Rev. B **95**, 125411 (2017).
[38] J. Dong, J. Zhao, and L. Liu, Near-field radiative heat transfer between clusters of dielectric nanoparticles, J. Quant. Spectrosc. Radiat. Transfer **197**, 114 (2017).
[39] J. Chen, B. X. Wang, and C. Y. Zhao, Near-field radiative heat transport between nanoparticles inside a Cavity Configuration, Int. J. Heat Mass Transf. **196**, 123213 (2022).
[40] J. Chen, B. X. Wang, and C. Y. Zhao, Scattering-type multi-probe scanning thermal microscope based on near-field thermal radiation, Int. J. Heat Mass Transf. **181**, 121869 (2021).
[41] A. Ott and S.-A. Biehs, Radiative heat flux through a topological Su-Schrieffer-Heeger chain of plasmonic nanoparticles, Phys. Rev. B **102**, 115417 (2020).
[42] B. X. Wang and C. Y. Zhao, Topological phonon polariton enhanced radiative heat transfer in bichromatic nanoparticle arrays mimicking Aubry-André-Harper model, Phys. Rev. B **107**, 125409 (2023).
[43] A. Ott, Z. An, A. Kittel, and S.-A. Biehs, Thermal near-field energy density and local density of states in topological one-dimensional Su-Schrieffer-Heeger chains and two-dimensional Su-Schrieffer-Heeger lattices of plasmonic Nanoparticles, Phys. Rev. B **104**, 165407 (2021).
[44] A. Ott and S.-A. Biehs, Topological near-field heat flow in a Honeycomb Lattice, Int. J. Heat Mass Transf. **190**, 122796 (2022).
[45] B. X. Wang and C. Y. Zhao, Radiative heat transfer mediated by topological phonon polaritons in a family of quasiperiodic nanoparticle chains, Int. J. Heat Mass Transf. **210**, 124163 (2023).
[46] S. R. Pocock, X. Xiao, P. A. Huidobro, and V. Giannini, Topological plasmonic chain with retardation and radiative effects, ACS Photonics **5**, 2271 (2018).
[47] B. X. Wang and C. Y. Zhao, Topological phonon polaritons in one-dimensional non-hermitian silicon carbide nanoparticle chains, Phys. Rev. B **98**, 165435 (2018).
[48] B. X. Wang and C. Y. Zhao, Topological photonic states in one-dimensional dimerized ultracold atomic chains, Phys. Rev. A **98**, 023808 (2018).
[49] B. X. Wang and C. Y. Zhao, Wideband tunable infrared topological plasmon polaritons in dimerized chains of doped-silicon nanoparticles, J. Appl. Phys. **127**, 073106 (2020).
[50] B. X. Wang and C. Y. Zhao, Topological quantum optical states in quasiperiodic cold atomic chains, Phys. Rev. A **103**, 013727 (2021).
[51] F. Herz and S.-A. Biehs, Thermal radiation and near-field thermal imaging of a plasmonic Su–Schrieffer–Heeger chain, Appl. Phys. Lett. **121**, 181701 (2022).
[52] M. Nikbakht and F. Bahmani, Topological edge states in nanoparticle chains: Isolating radiative heat flux, Phys. Rev. B **108**, 064307 (2023).
[53] F. Bahmani and M. Nikbakht, Topological phase-dependent thermalization dynamics in radiative heat transfer: Insights from a one-dimensional Su-Schrieffer-Heeger model, Opt. Express **32**, 1257 (2024).
[54] W. P. Su, J. R. Schrieffer, and A. J. Heeger, Solitons in Polyacetylene, Phys. Rev. Lett. **42**, 1698 (1979).
[55] M. S. Wheeler, J. S. Aitchison, J. I. L. Chen, G. A. Ozin, and M. Mojahedi, Infrared magnetic response in a random silicon carbide micropowder, Phys. Rev. B **79**, 073103 (2009).
[56] E. Tervo, Z. Zhang, and B. Cola, Collective near-field thermal emission from polaritonic nanoparticle arrays, Phys. Rev. Mater. **1**, 015201 (2017).
[57] M. Langlais, J.-P. Hugonin, M. Besbes, and P. Ben-Abdallah, Cooperative electromagnetic interactions between nanoparticles for solar energy harvesting, Opt. Express **22**, A577 (2014).
[58] M. Lax, Multiple scattering of waves, Rev. Mod. Phys. **23**, 287 (1951).
[59] B. X. Wang, C. Y. Zhao, Y. H. Kan, and T. C. Huang, Design of metasurface polarizers based on two-dimensional cold atomic arrays, Opt. Express **25**, 18760 (2017).
[60] L. Novotny and B. Hecht, *Principles of Nano-Optics*, 2nd ed. (Cambridge University Press, New York, 2012).
[61] D. Obana, F. Liu, and K. Wakabayashi, Topological edge states in the Su-Schrieffer-Heeger model, Phys. Rev. B **100**, 075437 (2019).
[62] X.-W. Xu, Y.-Z. Li, Z.-F. Liu, and A.-X. Chen, General bounded corner states in the two-dimensional Su-Schrieffer-heeger model with intracellular next-nearest-neighbor hopping, Phys. Rev. A **101**, 063839 (2020).
[63] R. Wang, M. Röntgen, C. V. Morfonios, F. A. Pinheiro, P. Schmelcher, and L. D. Negro, Edge modes of scattering chains with aperiodic order, Opt. Lett. **43**, 1986 (2018).
[64] B. X. Wang and C. Y. Zhao, Near-Resonant light transmission in two-dimensional dense cold atomic media with short-range positional correlations, J. Opt. Soc. Am. B **37**, 1757 (2020).
[65] B. X. Wang and C. Y. Zhao, Interferences and localization in disordered media with anisotropic structural correlations, J. Appl. Phys. **130**, 133101 (2021).
[66] Á. Buendía, J. A. Sánchez-Gil, and V. Giannini, Exploiting oriented field projectors to open topological gaps in plasmonic nanoparticle arrays, ACS Photonics **10**, 464 (2023).
[67] Y. Zhang, R. P. H. Wu, L. Shi, and K. H. Fung, Second-order topological photonic modes in dipolar arrays, ACS Photonics **7**, 2002 (2020).
[68] F. Liu and K. Wakabayashi, Novel topological phase with a zero berry curvature, Phys. Rev. Lett. **118**, 076803 (2017).
[69] B.-Y. Xie, H.-F. Wang, H.-X. Wang, X.-Y. Zhu, J.-H. Jiang, M.-H. Lu, and Y.-F. Chen, Second-order photonic topological insulator with corner states, Phys. Rev. B **98**, 205147 (2018).
[70] W. Feng, J. Wen, J. Zhou, D. Xiao, and Y. Yao, First-Principles calculation of Z2 topological invariants within the FP-LAPW formalism, Comput. Phys. Commun. **183**, 1849 (2012).
[71] J. Chen, C. Zhao, and B. Wang, Near-field thermal radiative transfer in assembled spherical systems composed of Core-Shell nanoparticles, J. Quant. Spectrosc. Radiat. Transfer **219**, 304 (2018).
[72] S.-A. Biehs, R. Messina, P. S. Venkataram, A. W. Rodriguez, J. C. Cuevas, and P. Ben-Abdallah, Near-field radiative heat

transfer in many-body systems, Rev. Mod. Phys. **93**, 025009 (2021).

[73] F. Herz and S.-A. Biehs, Generalized coupled dipole method for thermal far-field radiation, Phys. Rev. B **105**, 205422 (2022).

[74] M. Nikbakht, Radiative heat transfer in fractal structures, Phys. Rev. B **96**, 125436 (2017).

[75] E. Tervo, M. Francoeur, B. Cola, and Z. Zhang, Thermal radiation in systems of many dipoles, Phys. Rev. B **100**, 205422 (2019).

[76] M. Proctor, P. A. Huidobro, B. Bradlyn, M. B. De Paz, M. G. Vergniory, D. Bercioux, and A. García-Etxarri, Robustness of topological corner modes in photonic crystals, Phys. Rev. Res. **2**, 042038(R) (2020).

[77] L. Tsang, J. A. Kong, K.-H. Ding, and C. O. Ao, *Scattering of Electromagnetic Waves: Numerical Simulations*, 1st ed. (Wiley, New York, 2001).

[78] Y.-R. Zhen, K. H. Fung, and C. T. Chan, Collective plasmonic modes in two-dimensional periodic arrays of metal nanoparticles, Phys. Rev. B **78**, 035419 (2008).